Bachelor's thesis

Dynamics of Square-Waves in Time-Delayed Kerr Micro-Cavities

Submitted by

Lennart Papke

August 9, 2024

First examiner
PD Dr. Svetlana Gurevich

Second examiner
Prof. Dr. Julien Javaloyes

Universität Münster
Fachbereich Physik
Institut für Theoretische Physik

Contents

1. Introduction

Time-delayed systems (TDSs) are of central interest to the field of nonlinear physics, as well as to a great variety of applied sciences, because they consistently allow to model real life dynamical systems, that often exhibit time delays as a non-negligible aspect of their dynamics, very precisely.
Because of that, TDSs have been studied extensively in recent times, with applications ranging from climate models, which incorporate delayed feedback loops introduced by the limited speed, at which energy or mass can be transported within spatially extended systems [KKP17], to traffic models, in which time delays are generated by the finite reaction times of drivers [Oro+09], constituting a non-negligible factor to the dynamics of traffic flow. The mechanisms that introduce time delays to real world systems are ample and numerous more examples could be given, exemplifying the importance of time-delayed systems to the field of nonlinear sciences.
Mathematically, TDEs are typically modeled by a particular class of differential equations called delay differential equations (DDEs). The defining property of DDEs lies in the dependence of the rate of change of a system state $\dot{s}(t)$ on its own past, evaluated at $s(t-\tau)$. Both the dependence of the present state of a TDS on its past, as well as the time delay τ itself, that is characteristic for every TDS, can thus be consistently modeled by DDEs.
Within the scope of nonlinear physics, a field in which time-delayed systems can be easily realized is photonics. Here, time delays are often encountered in the context of laser systems and are introduced by different types of optical cavities, for instance in the form of ring cavities [Ike79] or external cavities [LK80]. In this thesis, the injected Kerr Gires-Tournois interferometer (KGTI) is examined as an exemplary case of a time-delayed system from photonics employing an external cavity. Within the KGTI, the characteristic time delay is introduced by an optical feedback loop, which extracts a portion of the injected electromagnetic-wave in the form of a laser propagating through the interferometer at time $t-\tau$, consequently reintroducing it into the system at time t, where τ thus denotes the time of delay characterizing the KGTI as a TDS.
The scope of the analysis of the KGTI system will lie on the formation of a certain class of periodic solutions called square-waves (SWs), which have already been shown to form within a great variety of time-delayed laser systems, for instance within injected semiconductor lasers [JAH15], semiconductor ring lasers [Li+16] or edge-emitting diode lasers [Gav+06]. Most generally, a square-wave describes a periodic profile, which is defined by a system amplitude switching between two or more alternating plateau values at a fixed frequency. In the case of an ideal SW, the transition between different plateaus is assumed to be instantaneous, thus resulting in a characteristic square shaped profile in the time domain. In reality, the mechanism responsible for the switch in amplitude is always associated with a finite switching time. Furthermore, the number of plateaus, which correspond to a fixed value of the system amplitude, may generally vary. In this thesis

however, the main focus will lie on square-waves with two or three plateaus. Regarding the analysis of SW solutions within the KGTI system, this thesis builds on the results of [Koc22] and [Koc+22], which have demonstrated that two-plateau square-wave solutions with a periodicity of approximately 2τ exist for certain parameter regimes within the KGTI system. In addition to that, it was also shown, that three-plateau square-wave solutions with a periodicity of approximately 3τ can be observed to exist alike within the KGTI system. While for the case of the period 2τ-SW solutions and their corresponding branches their mechanism of formation has been identified by [Koc22] in the form of super- and subcritical Hopf bifurcations describing their emergence as periodic solutions from the continuous wave regime of the KGTI, no such scenario has been identified for the period 3τ-SW solution branches. Instead, the period 3τ-SW solution branches were observed to be isolas, possessing no connection to the continuous wave branch or any other type of branch in that regard.

Subsequent to these results, the central aim of this thesis can be formulated, which is the analysis of three plateau square-waves with a periodicity of 3τ in time-delayed Kerr micro-cavities at the example of an injected Kerr-Gires-Tournois interferometer in the long delay limit. The focus of analysis will lie both on their mechanism of formation, as well as their corresponding evolution as the system parameters of the KGTI system are varied.

In addition to the 2τ- and 3τ-periodic SW solutions, it was demonstrated by [Koc22] that another class of SW solution branches, the so-called subharmonic solution branches can be observed to exist within the KGTI system. Expanding on these findings, in the second part of this thesis the subharmonic branches will be analyzed for two additional parameter sets with special regards to their stability, structure and their scenario of formation and annihilation. Furthermore, the evolution of SW profiles along the subharmonic branches will be examined.

The analysis will be conducted by utilizing a combination of direct numerical simulations, as well as numerical path-continuations. For that purpose, a Matlab implementation of the injected Kerr Gires-Tournois interferometer was performed, based on a delay algebraic equation description of the system.

In the following chapter, theoretical prerequisites are presented, which are required for the understanding of the analysis of nonlinear dynamical systems, as well as time-delayed systems described by delay differential equations and delay algebraic equations. Consequently, in section 2.6, the injected Kerr Gires-Tournois interferometer is introduced in detail. Correspondingly, a comprehensive description of the interferometer setup is given and system parameters, as well the governing equations of the KGTI system are introduced. Due to the infinite dimensional nature of systems governed by DDE's, the numerical methods needed to analyze them differ from nonlinear systems governed by regular ODEs or PDEs. The theoretical prerequisites that are needed to analyze TDSs numerically will therefore be introduced in detail in chapter 3 with special regards to the KGTI system.

2. Theoretical Preliminaries

2.1. Dynamical Systems

The field that concerns the analysis of the evolution of physical systems is called dynamics. Most generally, the continuous evolution of a physical system is given by a set of differential equations, relating the defining physical quantities of the system to each other, as well as their corresponding derivatives.

Typically, the evolution of a system depends upon several independent variables. In such instances, the system's dynamics are governed by a set of partial differential equations (PDEs). A popular example from physics is the Schrödinger equation, which describes the evolution of quantum systems in terms of a wave function $\psi(\vec{r}, t)$ in two independent variables; time and space. Systems that are governed exclusively by temporal evolution, as will be the case with the dynamical system analyzed in this thesis, are on the other hand characterized by a set of ordinary differential equations (ODEs), involving only ordinary derivatives of order n in time [Str94].

An n-dimensional system of ODEs, where its dimension is determined by the order of the highest derivative, can be characterized by a set of n first-order differential equations of the form

$$\begin{aligned} \dot{x}_1 &= f_1(x_1, ..., x_n, t, \boldsymbol{\mu}), \\ &\vdots \\ \dot{x}_n &= f_n(x_1, ..., x_n, t, \boldsymbol{\mu}). \end{aligned} \tag{2.1}$$

or abbreviated $\dot{\mathbf{x}} = \mathbf{f}(\mathbf{x}(t), t, \boldsymbol{\mu})$ using vector notation. Here x_1, ..., x_n describe the quantities that characterize the system exhaustively, for instance physical variables such as positions, velocities, field strengths et cetera, and/or corresponding derivatives with respect to time. Furthermore $\boldsymbol{\mu}$ denotes the potential dependence on a vector of parameters, while t denotes an explicit time-dependence. The solution $(x_1(t), x_2(t), ..., x_n(t))$ of Eq. (2.1) to a given initial condition $\mathbf{x}(t_0)$ is called trajectory and lives in n-dimensional phase space [Str94]. If a solution to Eq. (2.1) can be found analytically, then all trajectories to an arbitrary initial condition are known, allowing for a plenary understanding of the system's behavior for all t and arbitrary initial conditions.

Another important classification of dynamical systems concerns the power of $x_i(t)$ and its derivatives. Only if all x_i appear up to the first power and are no argument to a nonlinear function, the system is linear. Otherwise, it is to be classified as nonlinear.

In general, the analysis of nonlinear systems is extremely challenging and analytical solutions can only be found in exceptional cases [Str94]. Yet, by means of bifurcation-theory, fixed point analysis, as well as by numerical methods, as employed in this thesis and to be introduced in the following sections, the behavior of nonlinear systems may nevertheless be examined.

2.2. Attractors and Linear Stability Analysis

One way of analyzing the behavior of nonlinear dissipative systems without analytically solving them, is examining their behavior in the long-term limit, which is disregarding transient solutions, that the system exhibits as it converges towards an attractor. In this context, an attractor marks a subset of phase space, which is approached by a dynamical system in case its initial condition falls into the so-called basin of attraction of the attractor and the attractor is forward-invariant [Koc22].

In the presence of an attractor, a nonlinear dynamical system may thus reach a settled solution in the long-term limit, which is defined by the condition $\mathbf{f}(\mathbf{x}^*, t, \boldsymbol{\mu}) = 0$. In one-dimensional dynamical systems, $\mathbf{x}^*$ are called fixed points of the system and can be either classified as stable or unstable.

To determine the stability of fixed points, linear stability analysis can be employed, examining the behavior of a dynamical system in a fixed point solution subjected to a sufficiently small perturbation $\boldsymbol{\delta}(t)$ away from $\mathbf{x}^*$ [Str94] up to the first order. For a stable fixed point, the perturbation will decay, returning the system to $\mathbf{x}^*$. In case the fixed point is unstable, the perturbation will grow, eventually leaving the system in a different state than $\mathbf{x}^*$.

To formalize this, consider a small perturbation $\boldsymbol{\delta}(t)$ away from $\mathbf{x}^*$ leading to the perturbed solution $\tilde{\mathbf{x}}(t) = \mathbf{x}^* + \boldsymbol{\delta}(t)$. The time evolution of the perturbed solution up to the first order is given by

$$\dot{\tilde{\mathbf{x}}} = \dot{\mathbf{x}^*} + \dot{\boldsymbol{\delta}}(t) = \mathbf{f}(\mathbf{x}^*, t, \boldsymbol{\mu}) + (\nabla \mathbf{f})(\tilde{\mathbf{x}}, t, \boldsymbol{\mu})|_{\tilde{\mathbf{x}}=\mathbf{x}^*} \cdot \boldsymbol{\delta}(t) + \mathcal{O}(\boldsymbol{\delta}^2) \,. \tag{2.2}$$

With $\dot{\mathbf{x}^*} = \mathbf{f}(\mathbf{x}^*, t, \boldsymbol{\mu}) = 0$ per definition and the identification of the second term with the n x n dimensional Jacobian $\mathbf{J} = (\nabla \mathbf{f})(\mathbf{x}^*, t, \boldsymbol{\mu})$, this yields

$$\dot{\boldsymbol{\delta}}(t) = \mathbf{J}\, \boldsymbol{\delta}(t) \,. \tag{2.3}$$

With an exponential ansatz $\boldsymbol{\delta}(t) = \boldsymbol{\delta}_0 \cdot e^{\lambda \cdot t}$, Eq. (2.3) turns into the eigenvalue equation

$$\lambda_i \cdot \boldsymbol{\delta}_0 = \mathbf{J}\, \boldsymbol{\delta}_0 \,. \tag{2.4}$$

In the general case of a n-dimensional system, n complex eigenvalues of the Jacobian can be found that determine the stability of the fixed point $\mathbf{x}^*$. Since $\tilde{\mathbf{x}}$ evolves back to $\mathbf{x}^*$ as $\boldsymbol{\delta}(t)$ converges to zero, the fixed point is stable if $\mathrm{Re}(\lambda_i) < 0$ for all $i = 1, ..., n$ and unstable, if for at least one eigenvalue $\mathrm{Re}(\lambda_i) > 0$ is true.

However, for delay differential equations the corresponding eigenvalues may not be found easily, since the characteristic equation for linear stability analysis can be transcendental [Ern08] and there are infinitely many in the general case. Consequently, bifurcation-theory, as well as numerical methods that will be discussed in detail in the following sections, are needed to analyze it.

2.3. Bifurcation-Theory

A key method to the understanding of nonlinear dynamical systems that will be employed throughout this thesis, is bifurcation analysis. Bifurcations describe how dynamical systems abruptly transition between different qualitative behaviors, as system parameters are varied. This change in behavior affects both the nature of system solutions and their stability, as well as the existence and position of fixed points. The corresponding points in parameter space at which a fundamental change in system behavior occurs, are called bifurcation points [Str94].

To analyze (local) bifurcations in dynamical systems, bifurcation diagrams can be used, in which one or more control parameters of the system are plotted against the location of corresponding fixed points in phase space. Furthermore, the stability of the fixed points may be indicated. The result is a curve called a branch, that tracks the location of fixed points in phase space as system parameters are varied. Depending on the type of bifurcation, the branch may undergo different fundamental changes at the corresponding bifurcation points, such as splitting up, losing or gaining stability.

Each type of bifurcation can be described by a characteristic normal form, since the dynamics of every system, that undergoes a specific type of bifurcation, is equivalent in the limit of approaching the corresponding bifurcation point [Str94].

In the following sections, three main types of bifurcations are presented in detail that will be encountered in this thesis. For illustration purposes, a one-dimensional system with a single control parameter μ will be considered.

2.3.1. Saddle-Node Bifurcation

In a saddle-node bifurcation, a critical point is reached, where two fixed points are created, one stable and one unstable. The characteristic normal form describing the saddle-node bifurcation is

$$\dot{x} = \mu - x^2, \tag{2.5}$$

with the Jacobian $J = -2x$ obtained from differentiation of Eq. (2.5) with respect to x in accordance with the definition of the Jacobian reduced to the one-dimensional case.

In terms of the control parameter μ, three characteristic domains can be examined. For $\mu < 0$, Eq. (2.5) has no real solutions, meaning that no fixed points exist. At $\mu = 0$, a half-stable fixed point appears at $x = 0$. Since the Jacobian vanishes for $x = 0$ the only solution to the eigenvalue equation (2.4) is $\lambda = 0$, corresponding to infinitely slow dynamics of the system at this bifurcation point.

For $\mu > 0$, two fixed points emerge as solutions $x^* = \sqrt{\mu}$ and $x^* = -\sqrt{\mu}$ to Eq. (2.5). From Eq. (2.4), for the one-dimensional case it becomes immediately obvious that to $x^* = \sqrt{\mu}$ belongs a negative eigenvalue, meaning that $x^* = \sqrt{\mu}$ is stable, whereas to $x^* = -\sqrt{\mu}$ belongs a positive eigenvalue rendering it unstable. To sum up, at the bifurcation point of a saddle-node bifurcation the fundamental change in system behavior lies in the creation of two fixed point solutions, one stable and one unstable. The

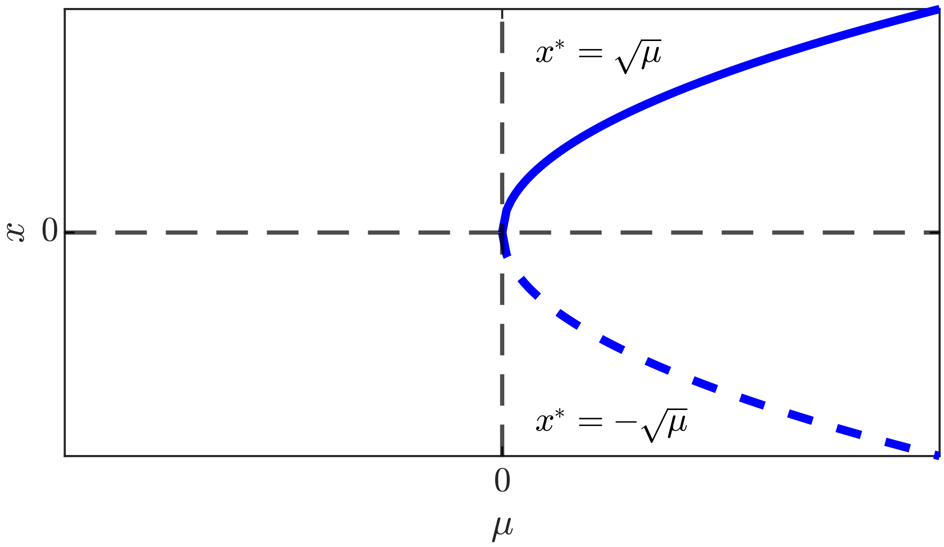

Figure 2.1: Bifurcation diagram of the saddle-node bifurcation derived from its characteristic normal form (Eq. (2.5)). For $\mu < 0$, no fixed points exist for the system. The saddle-node bifurcation occurs at $\mu = 0$, resulting in two fixed points for $\mu > 0$, one stable at $x^* = \sqrt{\mu}$ and one unstable at $x^* = -\sqrt{\mu}$.

corresponding bifurcation diagram is depicted in Fig. 2.1. The saddle node bifurcation also exists for periodic solutions in higher dimensions, which are particularly relevant for this thesis. In two dimensions, the so-called saddle-node bifurcation of cycles can be encountered, which is defined by the characteristic normal form

$$\begin{aligned} \dot{r} &= \mu r + r^3 - r^5 \\ \dot{\theta} &= \omega + br^2. \end{aligned} \tag{2.6}$$

As a critical value $\mu_c = -\frac{1}{4}$ is approached by the system parameter μ from the direction of $\mu > \mu_c = -\frac{1}{4}$, two limit cycles, one stable and one unstable, which both correspond to periodic solutions and exist for values $0 > \mu > \mu_c$, collide and annihilate; or coming from the other direction are born, when μ_c is reached [Str94]. This bifurcation is also called a fold bifurcation. This terminology will be used throughout this thesis.

2.3.2. Super- and Subcritical Hopf Bifurcations

Another type of bifurcation, which is encountered in the KGTI system analyzed in this thesis, is the so-called Hopf bifurcation. It can appear in nonlinear systems of any dimension n ≥ 2 and can be subdivided into two different types; super- and subcritical Hopf bifurcations. For the supercritical Hopf bifurcation, assume that the decay rate of a perturbation of a dynamical system in an equilibrium state may depend on an arbitrary system parameter μ. To formalize this, consider the characteristic normal form

$$\begin{aligned}\dot{r} &= \mu r - r^3 \\ \dot{\theta} &= \omega + br^2.\end{aligned} \tag{2.7}$$

For values $\mu < 0$, all trajectories starting with arbitrary values for r in phase space, begin to spiral inwards and reach a steady solution with an infinitesimal small oscillation frequency ω around the center of origin. This is due to the fact, that the first term in Eq. (2.7) governing the temporal evolution of r is always negative, given $\mu < 0$.
As μ approaches zero and finally supersedes it, the origin suddenly turns unstable. In turn a stable limit cycle at $r = \sqrt{\mu}$ is born. To sum up, the behavior for $\mu < 0$ corresponds to a dynamical system with a single equilibrium state, that is approached for arbitrary initial conditions. Perturbations from the equilibrium state decay, returning the system back to the steady state.

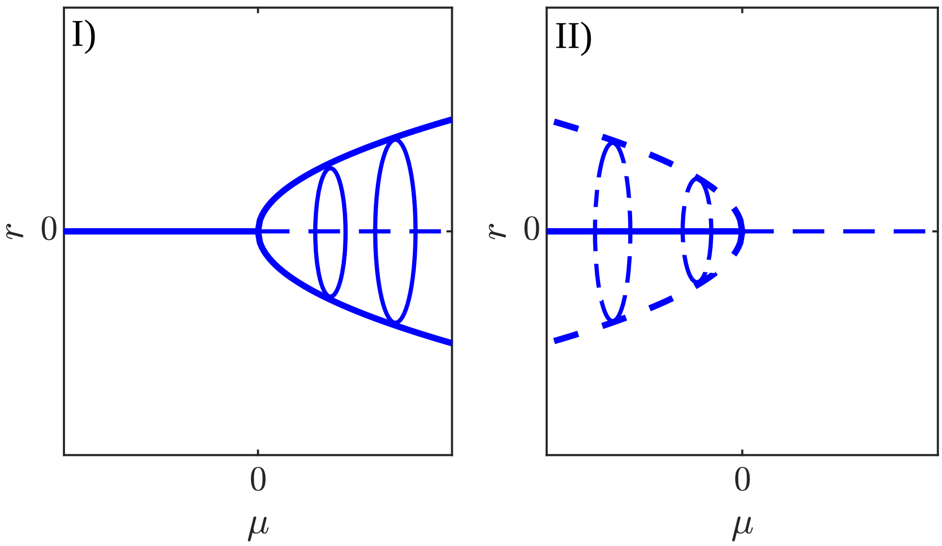

Figure 2.2: Bifurcation diagram of a Hopf bifurcation for the supercritical case (I) and the subcritical case (II) derived from their respective normal forms from Eq. (2.7) and Eq. (2.8). In the supercritical case, a stable fixed point at $r = 0$ loses stability in favor of a stable limit cycle, that exists for $\mu > 0$. In the subcritical case, a stable fixed point at $r = 0$ collides with an unstable limit cycle, as μ approaches zero, consequently turning unstable.

For $\mu > 0$, a single periodic solution becomes stable, while the formerly stable steady state turns unstable. This shift in stability means, that arbitrarily small perturbations may now displace the system from its steady state leading it towards the newly stable periodic solution. The bifurcation diagram corresponding to the supercritical Hopf bifurcation, that makes evident this behavior is depicted in Fig. 2.2 (I). From evaluating the Jacobian J in Cartesian coordinates, corresponding to the normal form 2.7, it can be shown that its eigenvalues $\lambda = \mu \pm i\omega$ cross the imaginary axis, when μ supersedes zero. This way the occurrence of a supercritical Hopf bifurcation can be characterized [Str94].

In analogy to the supercritical case, the subcritical Hop bifurcation can be characterized by the normal form

$$\begin{aligned} \dot{r} &= \mu r + r^3 - r^5 \\ \dot{\theta} &= \omega + br^2, \end{aligned} \tag{2.8}$$

albeit the cubic term now acts destabilizing. For $\mu < 0$, both a stable limit cycle and a stable fixed point at $r = 0$, as well as an unstable limit cycle between the two, exist. Increasing μ to $\mu = 0$, leads to the collision of the unstable limit cycle with the stable fixed point at $r = 0$ annihilating both in the process.

For $\mu > 0$, the stable limit cycle remains as the only stable solution of the system [Str94]. The bifurcation diagram corresponding to the subcritical Hopf bifurcation is depicted in Fig. 2.2 (II).

2.4. Time-Delayed Systems and Delay Differential Equations

In addition to ODEs and PDEs, a third class of differential equations called delay differential equations (DDEs) can be characterized. Since they govern the Kerr Gires-Tournois interferometer, whose analysis will be the focus of this thesis, their key properties shall be introduced in this section.

A key motivation for the consideration of DDEs is, that they can often be used to describe real world dynamical systems more accurately, than ODEs or PDEs allow for, since they incorporate time delays as their defining property, that are often a non-negligible aspect of the dynamic of real world systems. In its most general form, a DDE can be defined as

$$\dot{x}(t) = f\big(x(t),\ x(t-\tau_1), ...,\ x(t-\tau_N), t\big)\ , \tag{2.9}$$

where the delay system may depend on state vectors x of arbitrary dimension evaluated at N different points in time in the history of the system [Koc22]. A direct consequence of the fact, that the state of the system depends on its history evaluated at $t - \tau_i$, is that the initial condition has to be defined on a continuous interval $t \in [-\tau, 0]$ [Ern08] for every time delay τ_i. In that sense, even time-delayed systems (TDSs) with only a single time delay are infinite dimensional, since they require an infinite amount of initial conditions to define their state at a specific time t_0.

Consider for instance the basic example given by [Ern08] of a shower with water temperature T_0 at the control knob and water temperature T at the shower head. In this system, the delay is introduced by the time τ the water takes to travel from the portion of the control knob to the shower head. In consequence, both the rate of change of temperature at the shower head at time t, as well as the temperature itself depend on the position of the control knob evaluated at time $t - \tau$ and thus in the history of the system.

Another central mechanism for the generation of time delays in dynamical system is the

so-called delayed feedback loop. With this mechanism, a delay is generated by extracting a physical quantity from the system at time $t - \tau$, consequently reintroducing it back into it at time t. The state of the system at time t thus directly depends on its past. As will be explicated in detail in the next section, this marks the central mechanism to introduce a time delay in the Kerr Gires-Tournois interferometer.
Furthermore, systems governed by DDEs exhibit a plethora of different types of dynamics, among others pattern formation [YG14], temporal localized structures [JAH15] or most notably for this thesis, stable plateau solutions like square-waves [Koc22]. The formation of square-waves in particular, will be examined for the KGTI in this thesis. The relating theoretical preliminaries will be presented in the following section.

2.5. Square-Waves in Time-Delayed Systems

A square-wave (SW) is a special type of periodic solution, that is characterized by a system, whose amplitude switches between two or more alternating plateau values at a fixed frequency. The time spent at each plateau, defined by the so-called duty cycle, may vary for different types of SWs. For an ideal two-plateau SW, an even distribution is assumed, corresponding to a duty cycle of 50 %. Furthermore, a square-wave is characterized by the so-called rise- and fall times, which denote the time the amplitude of the system requires to switch between distinct plateau values.
For an ideal SW, an instantaneous switch between different plateau values is assumed, leading to a discontinuous progression of the system amplitude and thus creating the characteristic square shape in their temporal profile. For real world system however, the switching mechanism responsible for SW generation is always associated with a finite switching time.
Both due to theoretical interests as well as interests in possible applications of SWs in the context of optical and optoelectronical systems, SWs have emerged as a field of research of significant interest to theoretical physics, as well as applied sciences for practical applications such as optical clocks in signal processing [KAM10], communication systems [SWX13] and optical sensing [Ura+11].
While different mechanisms exist, that are responsible for the formation of SWs, as introduced in Chap. 1, time-delayed feedback loops have been shown to constitute a pivotal mechanism in the formation of SWs in the context of nonlinear time-delayed systems including the KGTI system. Since this chapter serves as an introduction to SWs, a detailed review of the central results for SW formation in the KGTI system by [Koc22] and [Koc+22], from which the leading question of this thesis will be derived, will follow in section 4.2.
In mathematical terms, the formation of SWs in time-delayed systems may be expected from their ability to produce antiperiodic output. The following derivation is based on [Koc22]. To make evident this this ability, consider

$$x(t) = e^{i\varphi} x(t - \tau). \tag{2.10}$$

While the solutions to this equation are τ-periodic for $\varphi = 0$, for $\varphi = \pi$ its solution $x(t)$ is antiperiodic with a switching time of τ. One class of solutions, that fulfill this conditions, are (ideal) two-plateau SWs with a duty cycle of 50 % and a total period of 2τ. To show that delay differential equations take the form of Eq. (2.10) in the long delay limit, consider

$$\epsilon\dot{x} = -x + f(\lambda, x(t'-1)), \tag{2.11}$$

where $t' = \frac{t}{\tau}$ was defined to express time in order of magnitude of the delay and $\epsilon = \frac{1}{\tau}$ serves as a smallness parameter. In the long delay limit $\epsilon \to 0$, the magnitude of the right hand side of the equation becomes negligible for any value of $\dot{x}$.

This corresponds to the defining property of a time-delayed system, being that the delay is long compared to all other dynamics of the system, as discussed in Sec. 2.4. Furthermore, assuming that f takes the form $f = e^{i\varphi}x(t'-1)$, the delay equation (2.11) indeed reproduces Eq. (2.10), illustrating how in the long-term limit a system governed by a DDE with a delay time τ induced by a feedback loop like the KGTI's, can be expected to exhibit SWs as a type of solutions.

Finally, the central condition for the formation of SWs, that lies in a switching time that is nearly instantaneous in comparison with the rest of system dynamics, can be derived from Eq. (2.11) by solving for $\dot{x}$ while assuming $\varphi = \pi$. This yields

$$\dot{x} = -\tau\big(x(t') + x(t'-1)\big), \tag{2.12}$$

an ordinary decay equation that strives for a minimum of $\tau\big(x(t') + x(t'-1)\big)$ given by $x(t') = -x(t'-1)$. Since the right hand side of the equation determines the magnitude of the minimization dynamics, in the case of the long-delay limit for $\tau \to \infty$, the process of minimization will be almost instantaneous.

In summary, this demonstrates how SWs can be expected to emerge in systems like the KGTI, governed by delay differential equations, when subjected to long delays and when the phase factor is set to $\varphi = \pi$ to allow for antiperiodic solutions.

2.6. Kerr Gires-Tournois Interferometer

In the following, the injected Kerr Gires-Tournois interferometer that is to be the focus of analysis of this thesis, will be presented in detail. This includes its setup, defining system parameters, as well as an explication of the governing system equations.

In Fig. 2.3, a schematic depiction of the KGTI is shown. As visible, the system can be subdivided into two compartments, a micro-cavity depicted on the left side, which constitutes its main functional component and an external cavity shown on the right side. The physical quantities of interest, that will be the focus of analysis in terms of the relevant nonlinear dynamics of the system, are the time dependent envelopes of the electric field $E(t)$ and $Y(t)$, where $E(t)$ denotes the electric field inside of the micro-cavity and $Y(t)$ the field inside of the external cavity. Starting with the micro-cavity, the following details can be explicated. The central component of the micro-cavity is a nonlinear Kerr medium with a radius of up to 100 nm [Koc+22] contained within the cavity. It is characterized by a cubic nonlinearity, which is responsible for the rich dynamics, that can be encountered within the KGTI system enabling the occurrence of genuine nonlinear effects, such as bistability [Sch+19b] [SJG22]. Furthermore, to the left

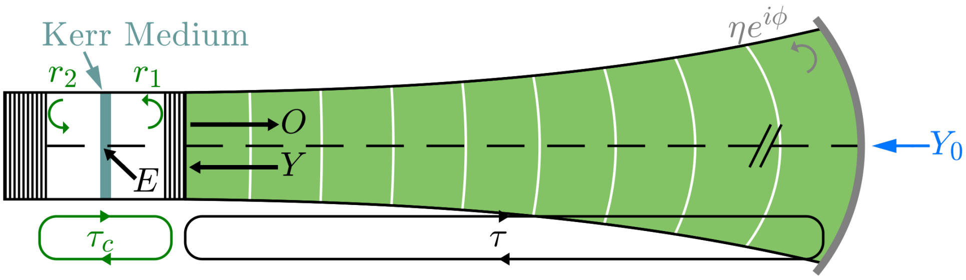

Figure 2.3: Schematic depiction of the Kerr Gires-Tournois interferometer (KGTI) [SJG22]. Its main functional component is a micro-cavity with round trip time τ_c, which inhabits a nonlinear Kerr medium, that enables the occurrence of genuine nonlinear effects within the interferometer. The micro-cavity is coupled with an external cavity with round trip time τ through a feedback mirror with refractive index $r_1 < 1$. In turn, the external cavity is injected with injection amplitude Y_0. Since it is assumed that $\tau_c << \tau$, the external cavity constitutes a feedback loop for the micro-cavity.

side the micro-cavity is closed off by a Bragg mirror, which is assumed to be perfectly reflecting with $|r_2| = 1$. This assumption leads to the light coupling efficiency, which is generally defined as $h = h(r_1, r_2) = (1+|r_2|)(1-|r_1|)/(1-|r_1||r_2|)$, to become $h(r_1, 1) = 2$ [Sch+19b] defining the so-called Gires–Tournois interferometer regime [GT64].
To the right side, the micro-cavity is separated from the external cavity by a semi-transparent Bragg-mirror with refractive index $r_1 < 1$. This allows for a coupling of both cavities. In total, the micro-cavity field $E(t)$ is determined by the effect of the nonlinear Kerr medium, as well as $Y(t)$ entering the micro-cavity from the external cavity due to the coupling of both cavities.
Continuing with the external cavity with a spatial extension in the centimeter range [Koc+22], the following characteristics can be detailed. On the right side, the external cavity is injected by an external injection with magnitude Y_0. Furthermore, from the side of injection, the external cavity is closed off by a feedback mirror with refraction index η, that reflects the output $O(t)$ originating from the micro-cavity adding a factor of $\eta e^{i\cdot\varphi}$ to $O(t)$ upon reflection, where $\varphi = \phi + \omega\tau$ describes the total accumulated phase of $O(t)$. Here, ϕ is the phase factor gained from reflection at the feedback mirror, while the factor $\omega \cdot \tau$ defines the contribution to the effective phase, gained from $O(t)$ traveling through the external cavity for a round-trip time of τ with injection frequency

ω [Koc+22]. Both η, as well as ϕ pose as material constants, that depend on the material properties of the feedback mirror used in the interferometer. In total, the electric field $Y(t)$ traveling through the external cavity is thus determined by the injection Y_0 and the phase modulated micro-cavity output $\eta e^{i \cdot \varphi} \cdot O(t)$, where the prefactor of $O(t)$ stems from the reflection, that occurred one round-trip before.
Since all mirrors are assumed to be lossless, the stokes relations can be utilized and given adequate scaling the output of the micro-cavity follows the basic relation [Koc+22]

$$O(t) = E(t) - Y(t). \tag{2.13}$$

Due to the separation of spatial dimension of the cavities, it can be assumed that $\tau_c << \tau$. τ_c is hence neglected in the following. The separation of timescales of τ and τ_c is central for the introduction of a time delay to the system. It allows for the external cavity to function as a time-delayed feedback loop for the micro-cavity, that accepts the portion of the electric field leaving the cavity at time $t - \tau$, consequently reintroducing it after the delay time τ at time t.
Since $\tau_c << \tau$, this delay is non-negligible for the dynamics of the system. As will be discussed in detail later in this thesis, the presence of the time-delayed feedback loop allows for the formation of SW solutions with a repetition rate, that appears as multiples of the time delay τ [Koc+22].
Finally taking all this information together the full equations, that govern the KGTI system are [Sch+19b] [MB05]

$$\dot{E}(t) = \left[-1 - i\delta + i \cdot |E(t)|^2\right] \cdot E(t) + h \cdot Y(t) \tag{2.14}$$
$$Y(t) = \eta e^{i\varphi} \cdot \left[E(t-\tau) - Y(t-\tau)\right] + \sqrt{1-\eta^2} \cdot Y_0. \tag{2.15}$$

While the exact derivation is out of the scope of this thesis, the system equations can be derived from first principles starting with the Maxwell equations, as demonstrated in detail by [MB05] and [Sch21].
Apart from the system parameters that have already been introduced, Eq. (2.14) additionally depends on the detuning $\delta = \omega_c - \omega$, which is the difference between the resonance frequency of the micro-cavity ω_c and the injection frequency ω.
While Eq. (2.15) is a direct consequence of the delay introduced by the external cavity acting as a feedback loop for the micro-cavity, it poses as an algebraic constraint for the system. Inserting it into Eq. (2.14) repeatedly, yields a single delay algebraic equation. The current rate of change of the electric field inside the micro-cavity $\dot{E}$ thus depends on all past round trips $Y(t - nt)$ with $n \in \mathbb{N}$ [Koc22]. The numerical methods used to analyze the KGTI system Eqs. (2.14) and (2.15), as well as preliminary results, will be explicated in detail in the next two chapters.

3. Numerical Methods

Since nonlinear differential equations can only be solved analytically in exceptional cases [Str94], numerical methods are needed to analyze them effectively. In this chapter, two central numerical methods, which will be employed throughout this thesis for the analysis of the KGTI system, will be introduced with special regards to their basic function as well as their scope and limits of application.

3.1. Implicit Euler Method for the Numerical Integration of Delay Differential Equations

Direct numerical simulations (DNSs) approximate the solution of an initial value problem for a given parameter set iteratively by discretization in both time and space. They are particularly suited for displaying transient behavior [Thi], since they can provide long-term simulations of the temporal evolution of nonlinear systems.

One such algorithm to calculate the evolution of a nonlinear system in time for a given initial condition, is called Euler's method [Str94] and can be applied to the general form of a one-dimensional DDE, as explicated in Sec. 2.4 Eq. (2.9). The derivation in this section is based on [Koc22]. Starting again with the definition of a one-dimensional DDE

$$\dot{x}(t) = f(x(t), x(t-\tau_1), ..., x(t-\tau_N), t), \tag{3.1}$$

with N delays $\tau_1, ..., \tau_N$, a time step h needed for the discretization is chosen, so that $\frac{\tau_i}{h} = m_i \in \mathbb{N}$ for $\forall \tau_i$. Furthermore, for the initial value problem, an initial value needs to be defined. In the case of a one-dimensional DDE, this takes the form of a discrete function

$$x_0(s) \quad \text{with} \quad s \in \{-\max_i(\tau_i), -\max_i(\tau_i) + h, ..., -h, 0\}. \tag{3.2}$$

For a more compact notation, the abbreviations $t = hn = t_n$ and $x(t_n) = x_n$ are defined. Under the approximation that the derivative $\dot{x}(t)$ remains constant over each time step h starting at a point x_n, the next point in discrete time can be approximated by the linear equation

$$x_{n+1} = x_n + h \cdot f(x_n, x_{n-m_1}, ..., x_{n-m_N}, t_n), \tag{3.3}$$

where $x_{n-m_i} = x(t_n - t_{m_i})$ are known from the initial condition (3.2). Eq. (3.3) describes a Taylor expansion of linear order in each point in discrete time.

For Euler's method, the local truncation error is of order $\mathcal{O}(h^2)$ and the global truncation error is of order $\mathcal{O}(h)$, which is defined by the difference of the final approximated value for $x(t_N)$ after N time steps and the true value the function takes at t_N.

While there exist more accurate algorithms such as fourth-order Runge-Kutta [Str94], increasing accuracy by taking into account not only the slope at the beginning of the time step h like Euler's method, but a weighted approximation of the slope at the beginning and the end of the interval h, as well as of the middle, in this thesis the implicit Euler's

method is used for numerical approximations, due to lower computational effort for calculating the evolution of the system over long time intervals.
In the following, the implementation of Euler's method, as it was employed to numerically solve the KGTI system in this thesis, will be derived. Starting with the system equations

$$\dot{E}(t) = \left[-1 - i\delta + i \cdot |E(t)|^2\right] \cdot E(t) + h \cdot Y(t) \tag{3.4}$$
$$Y(t) = \eta e^{i\varphi} \cdot \left[E(t-\tau) - Y(t-\tau)\right] + \sqrt{1-\eta^2} \cdot Y_0, \tag{3.5}$$

as introduced in Sec. 2.6, the abbreviations $E(t_{n+1}) = E_{n+1}$, as well as

$$\mathcal{L}_n = -1 + i(|E_n|^2 - \delta) \tag{3.6}$$

are defined. Applying Euler's method per Eq. (3.3) by discretization of time on system Eq. (3.4) yields

$$\frac{E_{n+1} - E_n}{\Delta t} = \mathcal{L}_n E_n + hY_n, \tag{3.7}$$

where h was renamed to Δt to avoid ambiguities with the system parameter h. Rearranging yields

$$E_{n+1} = E_n + \Delta t\,(\mathcal{L}E_n + hY_n). \tag{3.8}$$

In order to attain higher numerical accuracy, implicit Euler's method is introduced on both sides of the equation to the effect of replacing E_n, as well as Y_n, by their value in the center of the interval Δt. This gives

$$E_{n+1} = E_n + \Delta t\left(\mathcal{L}_n \frac{E_{n+1}+E_n}{2} + h\frac{Y_{n+1}+Y_n}{2}\right)\left(1 - \frac{\Delta t}{2}\mathcal{L}_n\right)E_{n+1} \tag{3.9}$$
$$= \left(1 + \frac{\Delta t}{2}\mathcal{L}_n\right)E_n + \frac{\Delta t}{2}h(Y_{n+1}+Y_n). \tag{3.10}$$

Rearranging one more time, the implicit Euler approximation for system Eq. (3.4) is

$$E_{n+1} = \frac{1}{1 - \frac{\Delta t}{2}\mathcal{L}_n}\Big[\left(1 + \frac{\Delta t}{2}\mathcal{L}_n\right)E_n + \frac{\Delta t}{2}h(Y_{n+1}+Y_n)\Big]. \tag{3.11}$$

Finally, applying Euler's method onto system Eq. (3.5) for the external cavity field and rounding $\frac{\tau}{\Delta t}$ to the next integer N, yields

$$Y_{n+1} = \eta e^{i\phi}(E_{n-N} - Y_{n-N}) + \sqrt{1-\eta^2}\,Y_0, \tag{3.12}$$

which can be inserted into the approximated expression (3.11) for Y_{n+1} and used for direct numerical simulations of the KGTI system.
For the simulations, an integrator implemented in Matlab was used. To conduct simulations, the following parameters require to be specified and handed over to the integrator. First, the time step Δt and the delay τ have to be defined. The discretization of time for the given delay time τ is given by the relation $\frac{\tau}{\Delta t} = N$, determining parameter N,

that equals the number of time steps fitting into the delay time. Since in the long-delay limit $\tau >> \Delta t$ is true, the resulting finite resolution still poses as a valid approximation. Furthermore, for every simulation an initial condition is needed for the integrator. This information is encoded in a N x 4 array, that contains the real and imaginary part for E and Y N-times respectively. The time difference between its first and last entry is exactly the delay time τ, as required for initial conditions for DDEs (see Sec. 2.4). The array containing the real and imaginary part for E an Y N-times, with a time difference of Δt, ensures the initial condition fits exactly the discretization in time, that is also used for the simulation ahead in time.
Conclusively, K simulation steps are specified, which determine the length of the simulation. During the simulation the initial condition contained in the N x 4 array is updated for each time step. The updated initial condition may thus be used to start new simulations, once the current simulation has concluded.

3.2. Numerical Path Continuation

Another central method for the analysis of nonlinear dynamical systems, which will be employed throughout this thesis, is numerical path continuation. It allows to track the evolution of the behavior of nonlinear systems and visualize the occurrence of bifurcations, by following system branches and their corresponding bifurcation points, as single or multiple system parameters are varied, in parameter space.
This allows to identify new branches and once located, numerical path integration also allows to follow bifurcation points in parameter space [Thi], as will be conducted in this thesis by means of two-parameter continuation of fold bifurcation points.
Numerical path continuation serves as a complementary method to direct numerics for the following reasons. First of all, direct numerics only allow to follow stable solutions. Numerical path continuations on the other hand allow to follow sections of branches, that consist of unstable solutions as well.
Furthermore, by means of direct numerical simulations alone, a systematic analysis of complex systems depending on multiple parameters is unfeasible, since DNSs only shed light on the behavior of the system for a particular parameter set and a given initial condition [Thi].
To conduct numerical path continuations, a single branch point, consisting of a settled solution $(\mathbf{x}_0, \mu_0)$ fulfilling the relation $\mathbf{f}(\mathbf{x}_0, \mu_0) = 0$, is required and can be obtained from DNS. Here, the dependence on parameters is made explicit with μ. Then, the parameter set μ_0 is varied, such that

$$\mu_0 \to \mu_0 + \Delta\mu = \mu_1, \tag{3.13}$$

with $\Delta\mu << \mu_0$. In order to get the adjacent settled solution to $\mathbf{x}_0$, now $\mathbf{x}_1$ fulfilling

$$\mathbf{f}(\mathbf{x}_1, \mu_1) = 0 \tag{3.14}$$

is required. To solve for $\mathbf{x}_1$, in this thesis the so-called pseudo arc-length method is employed. This method is employed, because it is suitable even for solving branches, which undergo saddle-node and/or fold bifurcations, as encountered later in this thesis, which can cause sharp turnarounds in the branches structure. This can lead to an ambiguity in what solution to follow, which poses challenging for algorithms, that cannot differentiate between those solutions.

The pseudo arc-length method can bypass this issue, by designating a unique value, the arc length s, to each point of the branch, which is monotonous along the entire branch, even in the case of saddle-node or fold bifurcations. The arc length s can be defined locally as

$$\Delta s^2 = \Delta \mathbf{x}^2 + \Delta \mu^2. \tag{3.15}$$

Once again exploiting a discretization in time, both $\Delta \mathbf{x}^2$ and $\Delta \mu^2$ can be approximated as

$$\Delta \mu^2 \approx (\mu_{n+1} - \mu_n) \frac{\partial \mu}{\partial s} \Delta s, \tag{3.16}$$

$$\Delta \mathbf{x}^2 \approx (\mathbf{x}_{n+1} - \mathbf{x}_n) \frac{\partial \mathbf{x}}{\partial s} \Delta s. \tag{3.17}$$

Inserting both terms into Eq. (3.15), then subtracting Δs on both sides, results in an additional equation

$$p(\mathbf{x}, \mu, s) \approx (\mu_{n+1} - \mu_n) \frac{\partial \mu}{\partial s} \Delta s + (\mathbf{x}_{n+1} - \mathbf{x}_n) \frac{\partial \mathbf{x}}{\partial s} \Delta s - \Delta s = 0, \tag{3.18}$$

where $\mu(s)$ is consequently treated as an additional variable depending on s. With Eq. (3.18) as an additional equation and defining $\mathbf{y} = (\mathbf{x}, \mu)$, the extended system can be defined as

$$\mathbf{E}(\mathbf{y}, s) = \begin{pmatrix} f(\mathbf{y}, s) \\ p(\mathbf{y}, s) \end{pmatrix} = 0, \tag{3.19}$$

where both f and p are required to vanish simultaneously. Starting with y_n, a solution to the extended system for a small step Δs at $s_{n+1} = s_n + \Delta s$, a predictor for the corresponding adjacent solution $\mathbf{y}_{n+1}$ can be obtained from calculating the tangent at point $(\mathbf{y}_n, s_n)$, using the Jacobian of the extended system. Then, Newtons method is used iteratively to calculate $\mathbf{y}_{n+1}$ for a fixed value of s_{n+1} to the desired accuracy. This method can be repeated to calculate the desired arc length s along the entire solution branch. For a more detailed and complete derivation see [Thi].

4. Preliminary Results

In this chapter, an overview over two fundamental types of solutions of the KGTI system Eqs. (2.14) and (2.15) will be presented, which have been examined in detail and constitute the foundation for this thesis. Since the central aim of this thesis concerns the analysis of 3τ-periodic SW solutions, the following sections will focus on preliminary results for SW solutions, as well as continuous wave (CW) solutions, which have been observed to form the basis for the formation of SWs from super- and subcritical Hopf bifurcations. Afterwards, preliminary results for 3τ-periodic SW solution branches will be discussed, that constitute the main concern of this thesis.

4.1. Continuous-Wave Solutions

To begin with, for $\varphi = 0$ the KGTI system exhibits a CW response, which becomes bistable for a certain range of values for Y_0 and δ, caused by the Kerr nonlinearity [Sch+19b] [SJG22]. The CW response constitutes the steady state solutions of the system. In the anti-resonant case, with $\varphi = \pi$ and the injection set precisely in-between two external cavity modes, bistability is lost and the intensity $I = |E(t)|^2$ can be calculated analytically from the implicit relation

$$Y_0^2 = \frac{1}{k_0}\left[k_-^2 + (I_s - \delta)^2\right] I_s \tag{4.1}$$

from the system Eqs. (2.14) and (2.15), where

$$k_\pm = \frac{1 \pm \eta\,(1-h)}{1 \pm \eta} \text{ and } k_0 = h\sqrt{\frac{1+\eta}{1-\eta}} \ . \tag{4.2}$$

Since it can be shown, that Y_0 is a monotonous function of I_s, Eq. (4.2) describing the anti-resonant scenario, indeed excludes bistability [Koc+22].

4.2. Square-Waves from Super- and Subcritical Hopf Bifurcations

Both analytically, as well as through a combination of numerical simulations and path continuations with the Matlab continuation tool DDE-BIFTOOL [ELR02], it can be shown that from the bistable CW regime, the formation of SWs in super- and subcritical Hopf bifurcations from the CW branch can be observed. For the numerical path integration, a DAE extension [SJG22] [HGJ21] for DDE-BIFTOOL was employed.
The resulting bifurcation scenario, together with the solution branches for CWs and SWs gained from both analytical, as well as numerical methods, are depicted in Fig. 4.1. Here, and for the rest of this thesis alike, thick lines represent stable solutions, whereas trim and dashed lines denote unstable solutions. To quantify system solutions and their evolution in parameter space, the measure $\langle |E|^2 \rangle$ is introduced and plotted on the y-axis against a control variable on the x-axis.

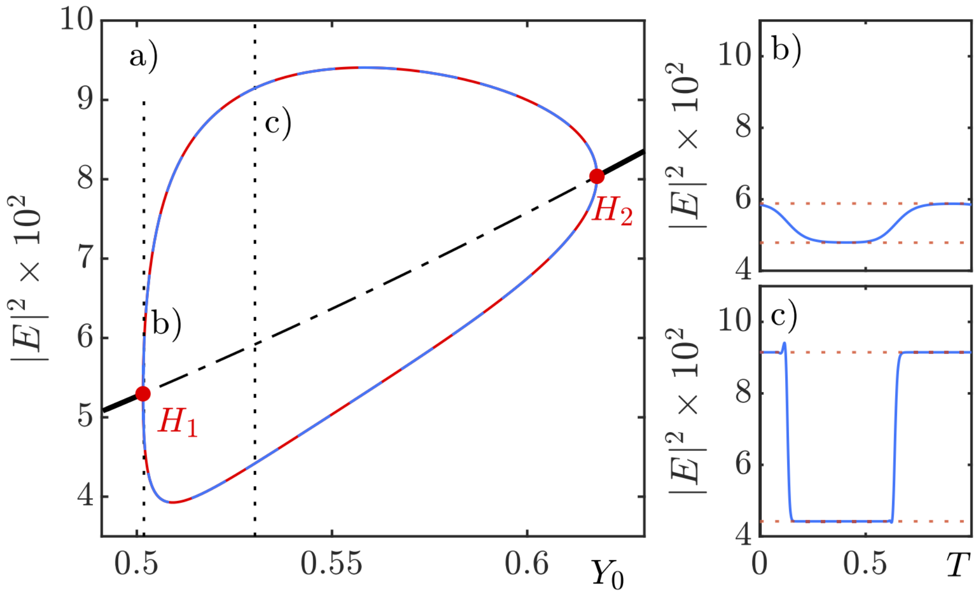

Figure 4.1: In a), the CW branch gained from Eq. (4.1) as a function of Y_0 is plotted together with the SW solutions obtained by means of numerical path-continuation (blue) and by analytical means (red). At H_1, the CW branch turns unstable in a supercritical Hopf bifurcation, giving rise to a SW branch, that reconnects to the CW branch in a supercritical Hopf bifurcation at H_2. In b), close to H_1 a sine-like periodic profile is visible, transforming into a fully developed SW depicted in c). The parameters are $(\delta, h, \eta, \varphi, \tau) = (0.1, 2, 0.9, \pi, 300)$ [Koc+22].

In the context of this thesis, Y_0 will predominantly take this role. The measure is calculated by evaluating the integral of the squared electric field of the solution over a full orbit for every solution along the branch.

Regarding the bifurcation scenario depicted in Fig. 4.1, it can be seen that at H_1, the CW branch (black) becomes unstable in a supercritical Hopf bifurcation giving rise to a stable SW branch, which ultimately reconnects with the CW branch in another supercritical Hopf bifurcation at H_2. In Fig. 4.1 b) and c), two profiles are depicted at two different injection values Y_0, as marked in panel a).

As evident, profile b), which was evaluated on the SW branch right after its separation from the CW branch, depicts a periodic solution similar to a sine function with a small amplitude. Along the branch, with increasing values of Y_0, this develops into a well developed two-plateau SW with a period of approximately 2τ and a duty cycle of 50 %. This mechanism of SW formation is already well established [Koc+22].

A second mechanism for the formation of SWs within the KGTI system can be observed, when the detuning is increased from $\delta = 0.1$ to $\delta = 0.2$. As depicted in Fig. 4.2, the bifurcation scenario changes drastically from Fig. 4.1, with the first Hopf bifurcation at H_1 turning subcritical and the SW branch undergoing a series of fold bifurcations,

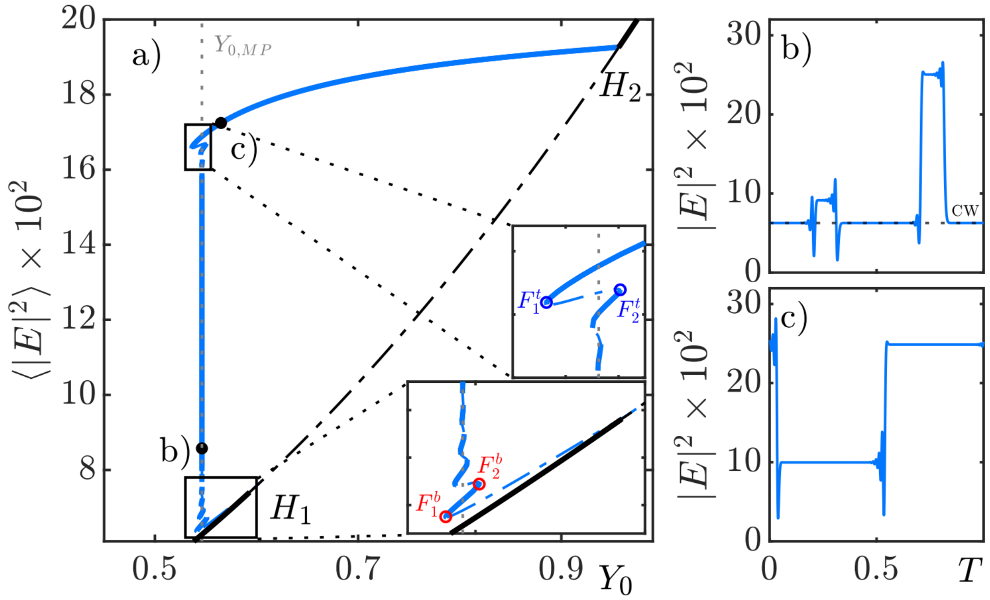

Figure 4.2: In a), the bifurcation scenario for an increased value of detuning from $\delta = 0.1$ to $\delta = 0.2$ is depicted. The resulting SW branch (blue) bifurcating from the CW branch (black) in a subcritical Hopf bifurcation, undergoes a series of fold bifurcations, which build a collapsed snaking structure connecting to the Maxwell line $Y_{0,\mathrm{MP}}$. In b), an exemplary profile is depicted exhibiting a complex shape and non-equidistant plateaus, which transforms into a fully developed two-plateau SW visible in c). Parameters are $(\delta, h, \eta, \varphi, \tau) = (0.2, 2, 0.9, \pi, 300)$ [Koc22].

that constitute a collapsed snaking structure, which is depicted in the lower zoom-box in Fig. 4.1 a). The two major folding points F_1^b and F_2^b are explicitly marked in the zoom-box. The collapsed snaking structure then feeds into a Maxwell line at $Y_{0,MP} \approx 0.54625$ [Koc22], which again concludes in a series of consecutive fold bifurcations, that connect to the upper portion of the SW branch, which finally reconnects to the CW branch in a Hopf bifurcation at H_2, that remains supercritical throughout the increase of detuning to $\delta = 0.2$.

Profile c), evaluated at the upper portion of the SW branch, confirms that from the collapsed snaking structures connecting to the CW branch at H_1, a fully developed two-plateau square-wave with a duty cycle of 50 % has emerged, whose amplitude decreases gradually as Y_0 is increased further, vanishing as a sinus-like function into the former steady state, as H_2 is approached, exactly like for the supercritical case for $\delta = 0.1$ [Koc+22]. Note that in contrast to profile c) in Fig. 4.1, substantial oscillatory tails can be observed in the vicinity of the transition layers between the two plateau values, which are caused by third order dispersion and the homoclinic snaking areas marked by the black zoom-boxes in Fig. 4.2 a) [Koc+22]. Since a very similar bifurcation scenario, constituted by two collapsed snaking structures, as well as a copulative Maxwell line, is encountered for 3τ-periodic SW branches, whose analysis is to be the primary focus of this thesis, the corresponding dynamics, which are exemplified by profile b), will be discussed in detail in the next chapter for the case of the 3τ-periodic SW branches.

4.3. Subharmonic Solutions

Another type of SW solution branches, which were observed to exist within the KGTI system, are the so-called subharmonic solution branches. Analogous to the period 2τ-SW branches presented in the last two sections, the subharmonic branches were observed to bifurcate from the CW branch of the corresponding parameter set in a cascade of n Hopf bifurcations, consequently reconnecting with it in another cascade of Hopf bifurcations. The defining property of the subharmonics is, that from the n-th Hopf bifurcation a

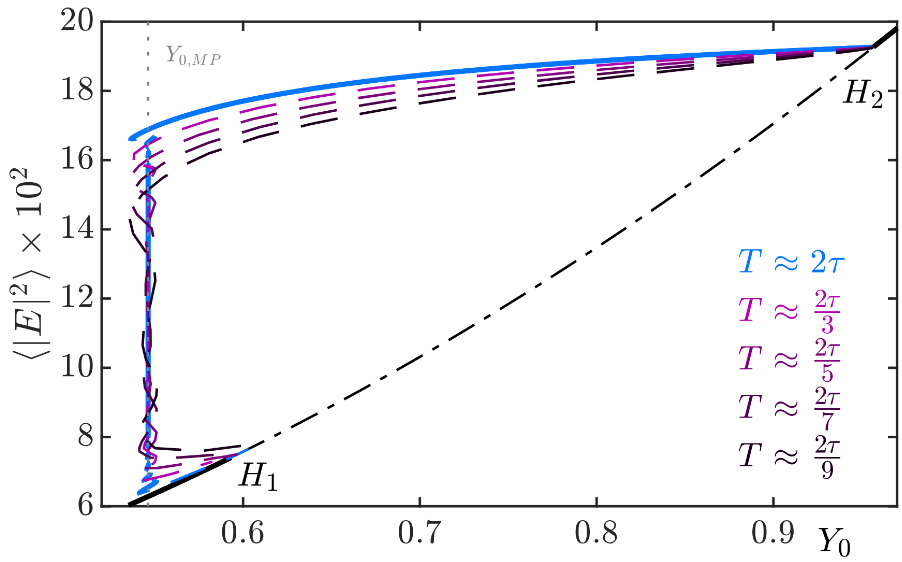

Figure 4.3: The first five subharmonic branches bifurcating from the CW branch (black) in a cascade of Hopf bifurcations consequently reconnecting with it in another cascade of Hopf bifurcations. Their corresponding periods match the expected pattern of $T = \frac{2\tau}{2n-1}$. Parameters are $(\delta, h, \eta, \varphi, \tau) = (0.2,\ 2,\ 0.9,\ \pi,\ 300)$ [Koc22].

SW branch with a periodicity of approximately $T = \frac{2\tau}{2n-1}$ is created [Koc22]. For the parameter set $(\delta, h, \eta, \varphi, \tau) = (0.2,\ 2,\ 0.9,\ \pi,\ 300)$, the first five subharmonic branches were explicitly observed by [Koc22]. The corresponding branches are plotted in Fig. 4.3. With a delay of $\tau = 300$, the periods of the subharmonic SW branches follow the expected pattern of $T = \frac{2\tau}{2n-1}$, as visible in the bottom right in Fig. 4.3. It can also be observed, that for $n > 1$ all of the subharmonic branches depicted in Fig. 4.3 are unstable. These results constitute the basis of analysis of subharmonic solutions within the KGTI system for an additional two parameter sets, conducted within the scope of this thesis. The results of the analysis will be presented in chapter 6.

5. Analysis of Period 3τ-SW Solutions

In this chapter, three branches of the KGTI system will be examined, which all correspond to periodic solutions featuring a triplet of alternating plateaus of approximately equal length τ. In correspondence to the results of [Koc22], they will thus be regarded to in abbreviated form as SW_3 solutions henceforth. Their analysis in the context of the KGTI system, as a time-delayed system with an injected Kerr micro-cavity, is to be the primary scope of the following sections.

The central aim of the analysis is to determine, how SW_3 solutions emerge in the KGTI system. This entails both to uncover their mechanism of formation and annihilation, as well as their corresponding evolution in parameter space.

In the last section, it has been shown that two main scenarios for the formation of period 2τ-SW branches have already been identified in both super- and subcritical Hopf bifurcations, generating SW branches that bifurcate from the CW branch and consequently reconnect with it. In direct contrast, the SW_3 solution branches presented in this section are isolated and share no connection to the CW branch or any other type of branch in that regard, in the parameter set at hand.

One of the central aims of this thesis will thus be to analyze the evolution of the SW_3 solution branches in parameter space and to verify, whether a parameter set can be located, where a connection to the CW branch, together with a subsequent separation instantiating them as isolated solutions, can be found. This would allow to attribute the formation of period 3τ-SWs to the same mechanism, that has already been identified for the formation of period 2τ-SW solutions, as presented in Sec. 4.2.

The second possibility that is to be regarded is, that their scenario of formation and annihilation, as well as their evolution in parameter space, is completely independent from the CW branch, or any other type of solution branch. In this case the aim of the analysis would turn to examine this alternative, independent scenario of SW_3 formation within the KGTI system.

The subsequent analysis will proceed as follows. First of all, three SW_3 solution branches will be presented and characterized according to their structure and corresponding dynamics. Then, a combination of one- and two-parameter continuation is employed to track the evolution of these branches and to examine the scenario of period 3τ-SW formation as well as annihilation in parameter space within the KGTI. Subsequently, central results are summarized. Note that all branches presented in chapters 5 and 6 are solutions to the KGTI system Eqs. (2.14) and (2.15).

5.1. Period 3τ-SW Solution Branches

The following three branches exhibiting SW_3 solutions were gained from one parameter variation of the system parameter Y_0 and will be referred to as $b_1^{3\tau}$, $b_2^{3\tau}$ and $b_3^{3\tau}$ respectively. This nomenclature follows that of [Koc22], being the first one to describe both $b_1^{3\tau}$ and $b_2^{3\tau}$. In contrast to the period 2τ-SW solutions, all three branches were found

within a parameter set with a significant increase in detuning from $\delta = 0.1$ and $\delta = 0.2$ respectively to $\delta = 0.8$. In turn, η was reduced from $\eta = 0.9$ to $\eta = 0.682$.
As with the CW and SW branches presented in chapter 4, Y_0 is chosen as a central control parameter throughout this thesis, since the amplitude of injection is, from an experimental standpoint, readily modifiable. Describing the dynamics of SWs in the KGTI system in terms of the injection amplitude, thus allows for an easier experimental reproduction of the results gained through this analysis.

5.1.1. SW_3 Solution Branch $b_2^{3\tau}$

To begin with, branch $b_2^{3\tau}$ is depicted in blue in Fig. 5.1 (I), with three exemplary profiles (II) - (IV) evaluated at three different points along the branch, marked with accordingly colored squares. Regarding the structure of the branch, as visible in panel (I), it is

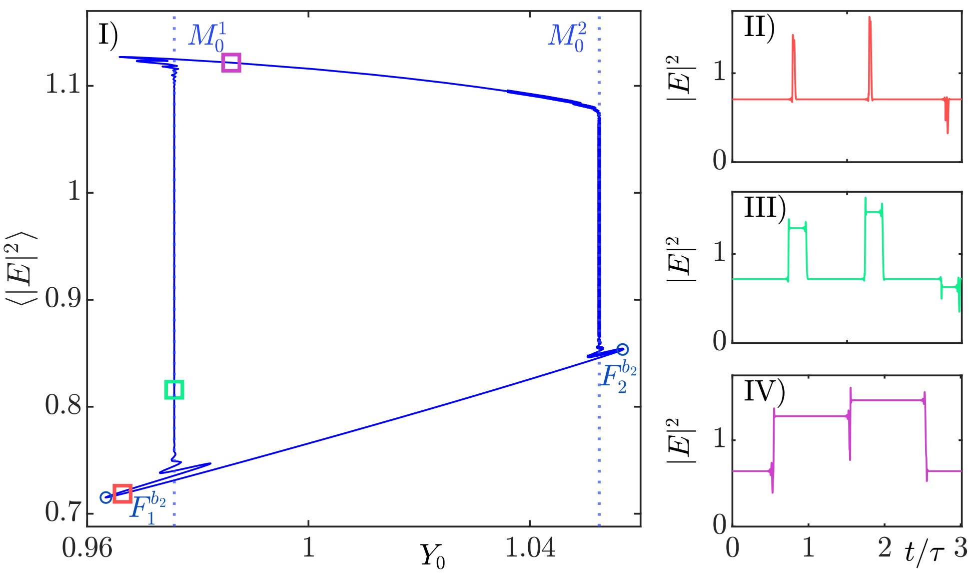

Figure 5.1: (I): Branch $b_2^{3\tau}$ in blue with three exemplary profiles depicted in panels (II) - (IV), which were evaluated at three different points marked by squares of matching color in panel (I). As visible, $b_2^{3\tau}$ is an isola possessing no connection to the CW branch. Profile (II), evaluated close to the onset of the collapsed snaking structure, takes the shape of a period 3τ-pulse solution, which gradually transforms into a fully developed SW_3 solution, as exemplified by the profiles plotted in panels (III) and (IV). Parameters are $(\delta, h, \eta, \varphi, \tau)$=(0.8, 2, 0.682, π, 300).

apparent, that $b_2^{3\tau}$ is an isola, which possesses no connection to the CW branch or any other neighboring branch, instantiating it as an isolated SW branch in the parameter regime at hand. The base of the branch is formed by two main folds spanned by the corresponding folding points $F_1^{b_2}$ and $F_2^{b_2}$. Following the two main folding points, it can be observed that $b_2^{3\tau}$ features multiple snaking structures, consisting of consecutive fold bifurcations, which collapse around two Maxwell lines at $M_0^1 \approx 0.9759$ and $M_0^2 \approx 1.0525$. Regarding the evolution of profiles along the branch, expanding on the results of [Koc22] and [Koc+22] for the case of the 2τ-periodic SW branches, the following analysis can be given.

Starting with the first profile in Fig. 5.1 (II) plotted in red, which is representative for the bottom section of the branch and was evaluated close to the onset of the collapsed snaking structure consisting of a series of fold bifurcations, it can be seen that the profile is characterized by three plateaus of equal width with a temporal extension much smaller than τ. In agreement with the 2τ-periodic SW solutions, unstable fronts can be observed for every plateau of the profiles in Fig. 5.1 in pairs of two. In the area of pronounced snaking directly following the main folding point $F_1^{b_2}$, the fronts are closer together and thus interact strongly with their oscillatory tails caused by third order dispersion (TOD) induced by the micro-cavity [Sch+19a], leading to the formation of stable solutions, where the fronts lock at distinct preferred distances close to the Maxwell line [Koc+22]. As exemplified by the profile in Fig. 5.1 (III), proceeding along the Maxwell line the pairs of fronts start to move away from each other leading to a decrease in interaction and thus a decline in snaking. The divergence of the fronts in turn leads to the increase of plateau width in the temporal domain as exemplified by the profile in Fig. 5.1 (III). Progressing the Maxwell line further, the three plateaus start to close in on each other and correspondingly the pair of fronts start to interact more strongly again, corresponding to an increase in snaking, as the top section of the branch is approached. As the homoclinic snaking at the top is reached, the plateaus finally converge leading to the formation of a well developed SW with three plateaus of approximate length τ, as exemplified by Fig. 5.1 profile (IV), which exhibits the defining properties of a SW_3 solution representative for the top section of the branch.

Moving along the upper section of the branch, by increasing the injection further, a steady decrease of plateau height of the SW_3 solution can be observed, while the overall structure is retained. Once the upper right snaking portion is reached and the the right Maxwell line M_0^2 is descended, the evolution gained during the ascension of M_0^1 is steadily reversed, until a profile of the type depicted in Fig. 5.1 (II) is restored upon reaching the bottom section of $b_2^{3\tau}$. Moving along the bottom section of the branch towards the branch point, that corresponds to Fig. 5.1 profile (II), the amplitude of the three pulses steadily declines for decreasing injection values Y_0, while the overall structure of a period 3τ-pulse solution is preserved.

To sum up, the lower section of $b_2^{3\tau}$ exhibits period 3τ-pulse solutions exemplified by the profile depicted in Fig. 5.1 (II), which transform into well developed SW_3 solutions, represented by the profile depicted in Fig. 5.1 (IV), as the collapsed snaking structure followed by the left Maxwell line M_0^1, is traversed. Transiting from the upper section to the lower section of $b_2^{3\tau}$ along the right Maxwell line M_0^2, the transformation from pulse solution to SW solution is reversed. This is due to the same mechanisms unfolding in reverse, fulfilling the requirement of continuity for each round trip along the branch.

5.1.2. SW_3 Solution Branch $b_3^{3\tau}$

In Fig. 5.2 (I), branch $b_3^{3\tau}$ is depicted in blue, with three exemplary profiles (II) - (IV) evaluated at three different branch points, which are marked with accordingly colored squares. In contrast to branch $b_1^{3\tau}$, which will be introduced in the following section,

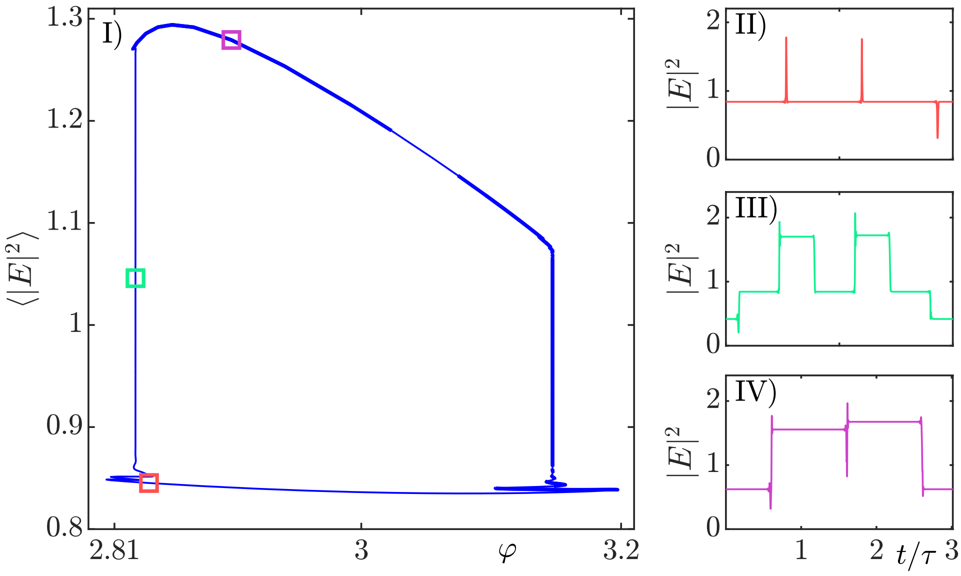

Figure 5.2: (I): Branch $b_3^{3\tau}$ in blue with three exemplary profiles depicted in panels (II) - (IV), which were evaluated at three different points marked by the squares of matching color in panel (I). The overall structure of $b_3^{3\tau}$ along the control variable φ closely resembles that of $b_2^{3\tau}$ in Y_0. As observable in panels (II) - (IV), the same functional structure leads to the same types of solutions, as well as to congruent dynamics for a round trip along the branch. Parameters are $(\delta, h, \eta, Y_0, \tau)$=(0.8, 2, 0.682, 1.050, 300).

and $b_2^{3\tau}$, branch $b_3^{3\tau}$ was gained from varying the phase feedback φ. Nevertheless the functional structure is completely analogous to that of branch $b_2^{3\tau}$, as evident from a direct comparison of Fig. 5.1 and Fig. 5.2. From profiles (II) - (IV) in Fig. 5.2, it becomes evident, that the similarities in structure to $b_2^{3\tau}$ lead to the same evolution of profiles along the branch.

Again, the upper portion, as exemplified by profiles (II) and (III) in Fig. 5.2, corresponds to fully developed SW_3 solutions, while the bottom section features solutions with three plateaus with a temporal extension much smaller than τ, that can thus be characterized as period 3τ-pulse solutions.

Furthermore, along the collapsed snaking structures, as well as the two Maxwell lines, congruent dynamics can be observed, which are defined by a pair of opposing fronts locked in a stable assembly, that move away from each other for the case of ascending the Maxwell line and that approach each other, when the Maxwell line is descended. This demonstrates, that the functional structure and corresponding dynamics of SW_3

solution branches of type $b_2^{3\tau}$, as observed by [Koc22] and [Koc+22], are not exclusive to the variation of the injection Y_0. Instead, the prototypical structure of branch $b_2^{3\tau}$ together with corresponding dynamics, can be observed within the KGTI system by variation of phase feedback φ as well, as made evident by the findings above.
In total, both for branch $b_2^{3\tau}$ as well as for $b_3^{3\tau}$, the observed transformation of the solutions along the collapsed snaking structure, as well as the Maxwell line, are in agreement with the transformations observed for the period 2τ-solution branches, detailed in chapter 4. The central difference is, that due to the isolation of $b_2^{3\tau}$ and $b_3^{3\tau}$ in the parameter set at hand, no transformation from a CW solution to a SW_3 solution via a sine-like periodic evolution of the CW state can be observed. As introduced in the beginning of this section, this motivates the central question, whether a parameter set can be located, where a connection to the CW branch can be detected, or an independent scenario of formation for the period 3τ-SW solutions is to be considered.
Before turning to the corresponding analysis, a third type of SW_3 solution branch is presented, that features a completely different functional structure, than $b_2^{3\tau}$ and $b_3^{3\tau}$. As will be shown in Sec. 5.2, this structure plays a central role in the mechanism of SW_3 formation within the KGTI system and is thus of central importance to this thesis.

5.1.3. SW_3 Solution Branch $b_1^{3\tau}$

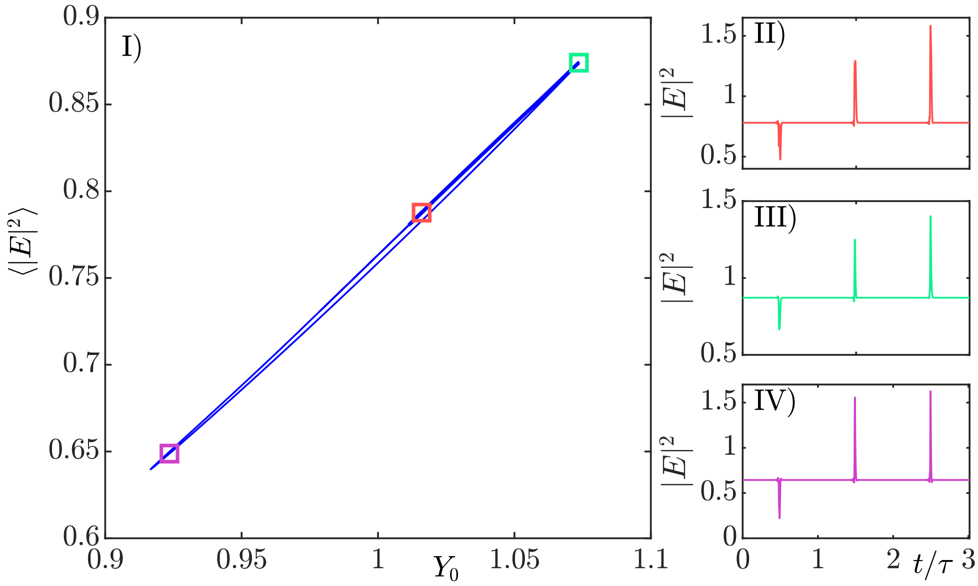

Figure 5.3: I): Branch $b_1^{3\tau}$ in blue with three exemplary profiles depicted in panels (II)-(IV). The profiles were evaluated at points marked by squares of matching color in panel (I). In contrast to branch $b_2^{3\tau}$ and $b_3^{3\tau}$, its structure is determined solely by two main folding points. Since no homoclinic snaking and no Maxwell line exist, that connect the upper section with the lower section of $b_1^{3\tau}$, both are inhabited by SW_3 pulse solutions, as visible in panels (II)-(IV). Parameters are $(\delta, h, \eta, \varphi, \tau)$=(0.8, 2, 0.682, π, 300).

In Fig. 5.3 (I), branch $b_1^{3\tau}$ is depicted in blue with three exemplary profiles (II) - (IV). In contrast to both period 2τ-SW branches detailed in Sec. 4, as well as to both SW_3 branches $b_2^{3\tau}$ and $b_3^{3\tau}$, $b_1^{3\tau}$ exhibits no homoclinic snaking and no Maxwell line connecting the upper section with the lower section of the branch. Instead, the entire structure of $b_1^{3\tau}$ is defined by two main folds.
Consequently, the evolution of profiles along the homoclinic snaking section, as well as the Maxwell line observable for branch $b_2^{3\tau}$ and $b_3^{3\tau}$, which leads to the formation of fully developed SW_3s living on the upper branch section, never occurs for branch $b_1^{3\tau}$. Hence, as evident from Fig. 5.3 (II) - (IV), the solutions can be characterized as period 3τ-pulse solutions along the entire branch, which are structurally equivalent to the solutions living on the lower section of $b_2^{3\tau}$ and $b_3^{3\tau}$. Like branch $b_2^{3\tau}$ and $b_3^{3\tau}$, branch $b_1^{3\tau}$ is isolated in the parameter set at hand. As will be shown in the following section, branches following the structural archetype of $b_1^{3\tau}$ play a central role in the scenario of formation and annihilation of SW_3 solutions within the KGTI system.

5.2. Two-Parameter Continuations

To analyze the evolution of the three SW_3 solution branches, presented in detail in the last section in parameter space and thus to determine the corresponding scenario of formation, two-parameter continuations were employed conducted with a DDE-BIFTOOL implementation in Matlab.
While two-parameter continuations were evaluated for all three branches, the results for branch $b_2^{3\tau}$ turned out to be most diversified and meaningful for the understanding of the scenario of SW_3 formation. The scope of this thesis will thus lie on the presentation of the results gained from two-parameter continuation of $b_2^{3\tau}$. Regarding the implementation of continuation by numerical means, the injection Y_0 was varied together with the system parameters of phase feedback φ, detuning δ and feedback strength η respectively, since Y_0 constitutes the central variable of dependence for branch $b_2^{3\tau}$.
Furthermore, the points that were selected for continuation were the two main folding points $F_1^{b_2}$ and $F_2^{b_2}$ marked in Fig. 5.1. This was done, because the two main folds are structure defining bifurcations, that initiate the homoclinic snaking scenario connecting to the two Maxwell lines of the branch. Thus tracking their evolution in parameter space is an effective way of tracking the functional structure of branch $b_2^{3\tau}$ as a whole. In particular, lower and upper boundaries for the existence of the two main folding points become evident from the fold diagrams gained from two-parameter continuation. These are of central interest, since the formation as well as the annihilation of the two main folds corresponding to the boundaries of existence, can be regarded as a strong hint for a fundamental change in branch structure. This is the case for the period 2τ-SW solution branches, where the homoclinic snaking directly follows the bifurcation from the CW branch. Hence, the continuation of the two major folding points is also an effective method to explicitly scan for parameter sets, in which a connection from the period

3τ-SW solution branch to the CW branch may be present. The following three sections are structured as follows. First the resulting fold diagrams gained from two-parameter continuation in the injection Y_0, together with the system parameters φ, δ, η for branch $b_2^{3\tau}$ will be presented with special regards to upper and lower limits of fold existence. Then, one-parameter continuations calculated in the areas of upper and lower fold existence, will be evaluated. This is done, because while fold diagrams only provide information about the location and existence of folds in parameter space, one-parameter continuations allow to visualize the specific modifications to the branches structure in the corresponding parameter set, as well as its stability and thus allow to visualize explicitly the mechanism of SW_3 formation within the KGTI system.

5.2.1. Two-Parameter Continuations in φ

The fold diagram gained from two-parameter continuation of the two main folds $F_1^{b_2}$ and $F_2^{b_2}$ of branch $b_2^{3\tau}$ in Y_0 and φ is depicted in Fig. 5.4. In the following, the functional

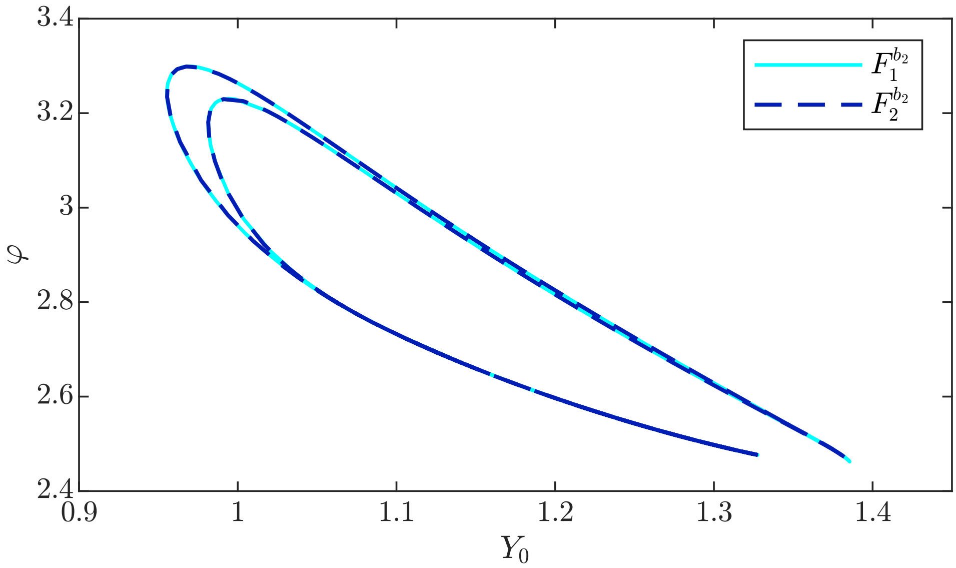

Figure 5.4: Two-parameter continuation of fold $F_1^{b_2}$ (cyan) and fold $F_2^{b_2}$ (blue-dashed) in the system variables φ and Y_0. The resulting fold diagram forms a closed structure in $(\varphi - Y_0)-$space. Furthermore, an upper as well as a lower boundary for fold existence can be detected. While the upper boundary at $\varphi \approx 3.3$ consists of two loops, the lower boundary is made up of two hooks and is located at $\varphi \approx 2.5$. Parameters are (δ, h, η, τ)=(0.8, 2, 0.682, 300).

structure of the diagram will be analyzed. Firstly, $F_1^{b_2}$ and $F_2^{b_2}$ overlap completely along the entire path in parameter space. This does not mean, that both folds coexist at every point in parameter space, but can be explained by the fact that the branch is closed, so at some point the folds merge and then annihilate. Regarding the structure of the fold diagram, it can be observed that it forms a closed loop in $(\varphi - Y_0)-$space, which is to be

expected due to the phase feedback φ being a periodic variable. Because of that, both an upper boundary as well as a lower boundary for the existence of $F_1^{b_2}$ and $F_2^{b_2}$ can be found, as evident in Fig. 5.4.
While the upper limit of fold existence can be located at $\varphi \approx 3.3$, the folds cease to exist at a lower limit of $\varphi \approx 2.5$ respectively. This demonstrates that SW_3 solutions are not unique to the parameter set $\varphi = \pi$ considered by [Koc22], but exist for a wide range of values in φ. The widest extent of the folds can be observed for values around $\varphi = 3.1$, just below $\varphi = \pi$, where branch $b_2^{3\tau}$ was calculated.
To examine the mechanisms of formation and annihilation of the two main folds $F_1^{b_2}$ and $F_2^{b_2}$, as well as the evolution of branch $b_2^{3\tau}$ in the system parameters φ and Y_0, one-parameter continuations in Y_0 with φ at fixed values were employed at different regions of the fold diagram. To begin with, the region incorporating the upper boundary of fold existence consisting of two looping structures was analyzed as depicted in Fig. 5.5. In

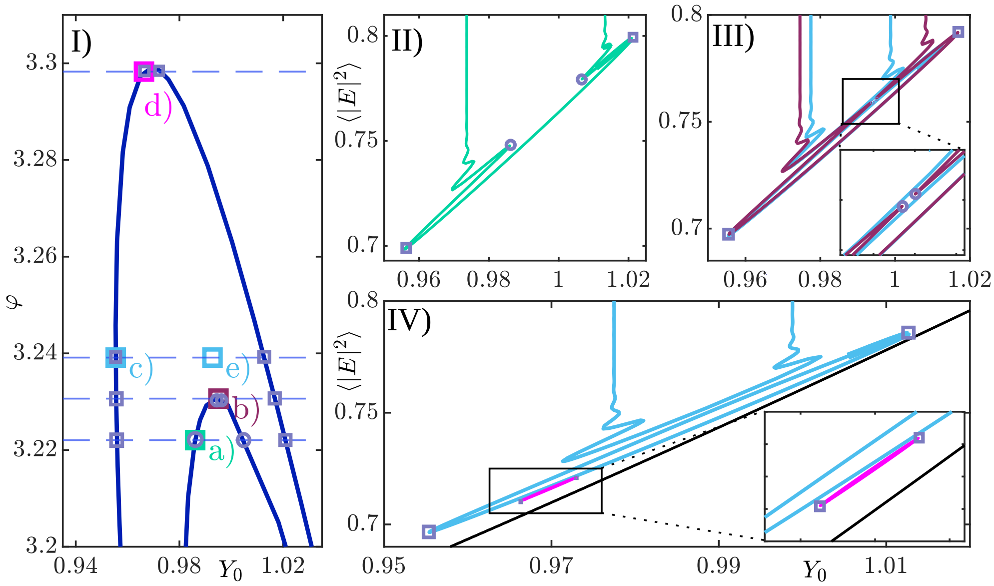

Figure 5.5: (I): Zoom-in on the upper limit of the fold diagram consisting of two loops. Points a) - e) mark the starting points for one-parameter continuations in Y_0 with φ at fixed values. The resulting branches are depicted in panels (II) - (IV), matching the color of the corresponding starting points. Within the branches, pairs of folds belonging to the outer loop of fold existence are marked by squares, while pairs of folds belonging to the inner loop are marked by circles. Since branch c) and e) belong to the same parameter set, they share the same color. Parameters are (δ, h, η, τ)=(0.8, 2, 0.682, 300).

order to do so, four representative points a) - d) were selected along the inner and outer loop of fold existence, where one-parameter continuations were started in Y_0 with φ at a constant value.
The resulting branches are portrayed in Fig. 5.5 (II) - (IV). Their color matches the color of their corresponding starting points marked by the four squares. To begin with, profile

a) colored in green was evaluated on the inner loop of the fold diagram at $\varphi \approx 3.222$ at point a). It mirrors perfectly the structure of branch $b_2^{3\tau}$ evaluated at $\varphi = \pi$, characterized by an upper and a lower section connected by two collapsed snaking structures, which are in turn connected by a Maxwell line. This demonstrates, that coming from $b_2^{3\tau}$ up until $\varphi \approx 3.222$ no fundamental change in branch structure has occurred.
As made evident by Fig. 5.5 (I) and (II), all four folds that lie on the intersection of the blue dashed line with the starting point of branch a), do not belong to different branches, but all appear as features of branch a). By comparison of Fig. 5.5 (I) and (II), it can be seen, that the pair of folds belonging to the outer loop, which is marked by two squares, corresponds to the outermost pair of folds of branch a). Likewise, the pair of folds belonging to the inner loop, marked by two circles, corresponds to the inner most pair of folds of branch a).
To examine the evolution of branches along the inner loop, the structure of branch b) colored in dark-red can be compared directly to the structure of branch a), as branch b) was evaluated close to the turning point of the inner loop, as depicted by Fig. 5.5 (I). As to be expected from the pathway of the fold diagram, the evolution from branch a) to branch b) is characterized by the convergence of the inner pair of folds, while the overall branch structure is retained.
In the zoom-box in Fig. 5.5 (III), it can be seen that the inner pair of folds, again marked accordingly by to circles, can be observed to have almost collided in branch b). This behavior is in agreement with the position of branch b), as it was calculated in direct proximity to the turning point of the inner loop. As determined by the fold diagram in Fig. 5.5 (I), when φ is increased further and the turning point of the inner loop is reached, the inner pair of folds finally collides and annihilates.
The effects of this collision and consequent annihilation of the two folds is made evident by comparison of branches b), c) and e). Since branch c) and e) share the same parameter set, both are plotted together in Fig. 5.5 (IV) in light blue.
From comparison of branch b) with branch c), it becomes evident that the annihilation of the inner pair of folds leads to a separation of the lower section of branch b) from the upper section as a closed isola. While in Fig. 5.5 (III) the almost closed isola can be observed to still be a part of branch b), in Fig. 5.5 (IV) it can be observed to have fully closed forming an independent branch, which can be identified with branch c).
Since the inner pair of folds have merged in the annihilation process, the structure of the remaining isola now depends only on the remaining outer pair of folds, which are marked by two squares and belong to the outer loop of the fold diagram. The observed structure of branch c) closely mirrors that of branch $b_1^{3\tau}$.
In contrast, the upper section of branch b) continues to exist independently from the closed isola and can be identified with branch e) in Fig. 5.5 (IV). Since branch e) features none of the folds present in the fold diagram in Fig. 5.5 (I), it had to be located by tracking a point from the upper section of branch b) under variation of φ, until φ assumed the same value as defined by the parameter set of branch c). In this parameter

set, profile e) was calculated from one-parameter continuation in Y_0. As a result, branch c) and e) share the same parameter set and can thus be compared directly to each other. This is also why they were plotted using the same color. As observable in Fig. 5.5 (IV), branch c) and branch e) indeed share no connection to each other, despite existing in the same parameter set.

To illustrate the relationship between branch b) on the one side, and its successors branches c) and e) on the other side, all three branches were plotted together in Fig. 5.5 (III). This plot illustrates even more clearly, that branch e) corresponds to the upper part of branch b), which continues to exist independently after the inner pair of folds annihilate, while the lower section spanned by the two outer folds corresponds to branch c), which separates as a closed isola in the same instance.

Furthermore, from the structure of branch e) depicted in Fig. 5.5 (IV), it can be hypothesized that the same mechanism of isola separation is likely to repeat itself, since the next pair of inner folds can be observed to approach each other in branch e), while the corresponding outer pair of folds can be observed to shape another isola solution, mirroring the evolution observed from branch a) to branch b) respectively. This isola solution may consequently separate from branch e) in another annihilation of folds. In a broader scheme of things, this suggests, that the formation of SW_3 isolas from fold annihilation constitutes a typical mechanism of SW_3 branch formation within the KGTI system.

With the analysis of branch evolution along the inner loop concluded, now the evolution along the outer loop of the fold diagram depicted in Fig. 5.5 (I) will be examined, which is represented by branches c) and d), where d) colored in violet was evaluated very close to the turning point of the outer loop of fold existence. By direct comparison of branch c) and branch d) in Fig. 5.5 (IV), it can be observed that with increasing values of φ the extent of the branches decreases, while their characteristic isola structure is retained. Evidently the extent of branch c) and d) is determined completely by the behavior of convergence of the pair of folds, which constitute their structure in $(\varphi - Y_0)-$space. For that reason, it can be argued that as the upper limit of fold existence is approached, the branches corresponding to the outer loop steadily decrease in size and finally vanish in the limit of reaching the turning point, as illustrated by the evolution from branch c) to d). Together with the fact that by going from branch c) to d), no convergence of the two branches to the CW branch in black can be observed, as evidently displayed in the zoom-box in Fig. 5.5 (IV), it can be concluded that the solutions belonging to the outer loop do not emanate from the CW branch of the corresponding parameter regime. Instead, an independent scenario of formation and consequent annihilation can be observed, that is constituted by the separation of an isola solution from the main branch, that consequently vanishes as the structure defining pair of folds of the isola converges in $(\varphi - Y_0)-$space. With the analysis of the upper limit of fold existence complete, now the evolution of SW_3 branches along the middle and lower section of the fold diagram will be examined. This corresponds to values between $\varphi \approx 3.2$ up until $\varphi \approx 2.45$, as visible in Fig. 5.4. As already known, between $\varphi = 3.2222$ and $\varphi = \pi$, branches of type $b_2^{3\tau}$ can be observed. When φ is lowered continuously approaching the lower limit of fold existence, the fold diagram depicted in Fig. 5.4 predicts the convergence of the inner left with the outer left folding points, as well as the the inner right with the outer right folding points.

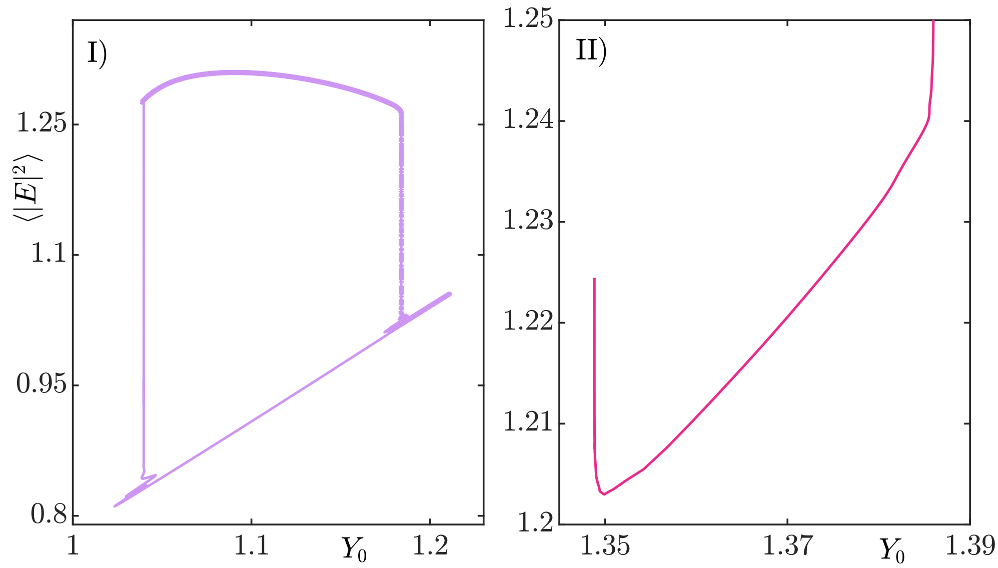

Figure 5.6: The two branches depicted in panel (I) and (II) were gained from one-parameter continuation in Y_0 with φ at a constant value illustrating the evolution of branch $b_2^{3\tau}$ as the lower limit of fold existence is approached. While the branch in panel (I) ($\varphi = 2.85$) retains the structure of $b_2^{3\tau}$, the branch in panel (II) ($\varphi = 2.462$) is characterized by a loss of all folds. Note: The continuation of the branch from panel (II) could not be finished due to difficulties with DDE-BIFTOOL. Parameters: (δ, h, η, τ)=(0.8, 2, 0.682, 300).

In Fig. 5.6, two branches that visualize this evolution are depicted. To begin with, the branch plotted in violet in Fig. 5.6 (I) was calculated at $\varphi \approx 2.85$ in the middle section of the fold diagram. As visible, the original branch structure from branch $b_2^{3\tau}$ is largely retained.

In contrast, the branch plotted in light-red in Fig. 5.6 (II) was evaluated right at the lower limit of fold existence at $\varphi \approx 2.462$. As evident, due to the collision of inner and outer folds with each other as predicted by the fold diagram, again a fundamental change in branch structure has occurred. Interestingly, not only the two pairs of folds, which were tracked by the fold diagram, have vanished from the branch. Instead, all folds have vanished leading to the dissolution of the collapsed snaking structures on both sides of the branch. Conclusively, as evident from Fig. 5.6 (II), just like in the upper limit of fold existence, no connection with the CW branch can be observed in the lower limit of fold existence. Instead, an independent scenario of SW_3 branch evolution is encountered. With that, the evolution of $b_2^{3\tau}$ regarding its two main folding points is completely understood in $(\varphi - Y_0)-$space. In between the lower and upper limit of fold existence, the known structure of $b_2^{3\tau}$ is retained. By examination of the upper and lower limit of fold existence, both of which causing a fundamental change in branch structure, no bifurcation scenario to the CW branch can be detected, which would allow to attribute the formation of period 3τ-SW solutions to the same mechanism, that has already been identified for the formation of period 2τ-SW solutions. Instead, both for the upper- as well as the lower limit of fold existence, an independent scenario of SW_3 branch formation and annihilation is encountered.

Approaching the upper limit of fold existence, it could be observed that an SW_3 isola separates from the main branch of type $b_2^{3\tau}$, caused by the collision of the inner pair of folds corresponding to the inner loop of the fold diagram. The separated SW_3 isola was then observed to vanish independently from the CW branch, as its structure defining pair of folds, corresponding to the outer loop of the fold diagram, converges in $(\varphi - Y_0)-$space. Additionally, the main branch from which the isola separates, was observed to continue to exist independently. From its structure it was hypothesized, that

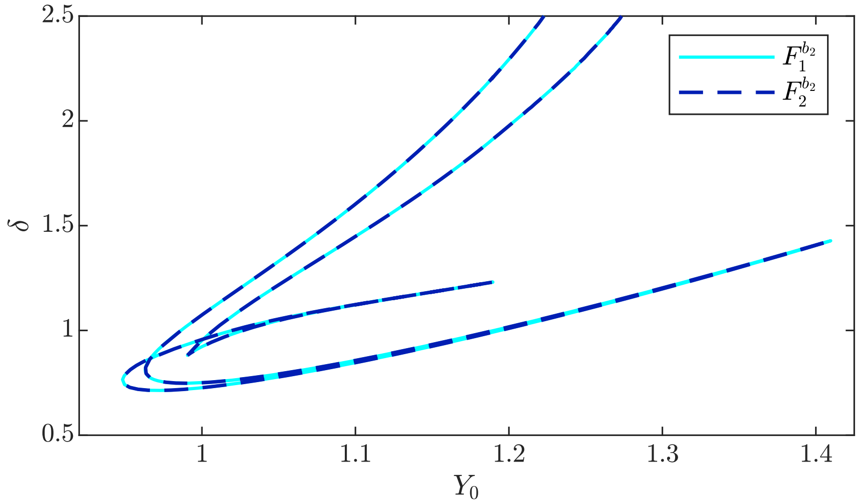

Figure 5.7: Two-parameter continuation of folds $F_1^{b_2}$ and $F_2^{b_2}$ in the system variables of injection Y_0 and detuning δ. In contrast to the fold diagram gained from varying φ, it features a much more intricate structure with multiple crossings and sharp hooks. For physically meaningful values $\delta < 2.5$, no upper limit of fold existence can be observed, while a lower limit of existence can be located for values $\delta < 0.75$ and $Y_0 < 0.95$. Parameters are (h, η, φ, τ)=(2, 0.682, π, 300).

the observed mechanism of SW_3 isola separation is likely to repeat itself, possibly until no more folds remain. A branch in agreement with this scenario was directly observed in the lower limit of fold existence, as depicted in Fig. 5.6 (II).

5.2.2. Two-Parameter Continuations in δ

Analogous to the methodology of Sec. 5.2.1, this section concerns the analysis of the fold diagram gained from two-parameter continuation of branch $b_2^{3\tau}$s two main folds $F_1^{b_2}$ and $F_2^{b_2}$ in Y_0 and detuning δ. The resulting fold diagram is depicted in Fig. 5.7. As can be seen, concerning the limits of fold existence for physically meaningful values $\delta < 3$, no upper boundary of existence is observable. An existence of such a boundary for values δ greater than three can not be excluded. A lower boundary for the existence of the folds $F_1^{b_2}$ and $F_2^{b_2}$ can be observed for values $\delta < 0.75$ and $Y_0 < 0.95$.
In direct comparison to the fold diagram gained from two-parameter variation of Y_0 and φ (see Fig. 5.4), the fold diagram gained from varying Y_0 and δ does not form a closed structure in $(\delta - Y_0)-$space, which is to be expected since δ is a non-periodic variable. Furthermore, it can be observed that varying δ instead of φ leads to a much more complicated structure of fold behavior in parameter space with multiple crossings and sharp hooks in the area of Y_0 between 0.9 and 1 and δ between 0.5 and 1. To examine the

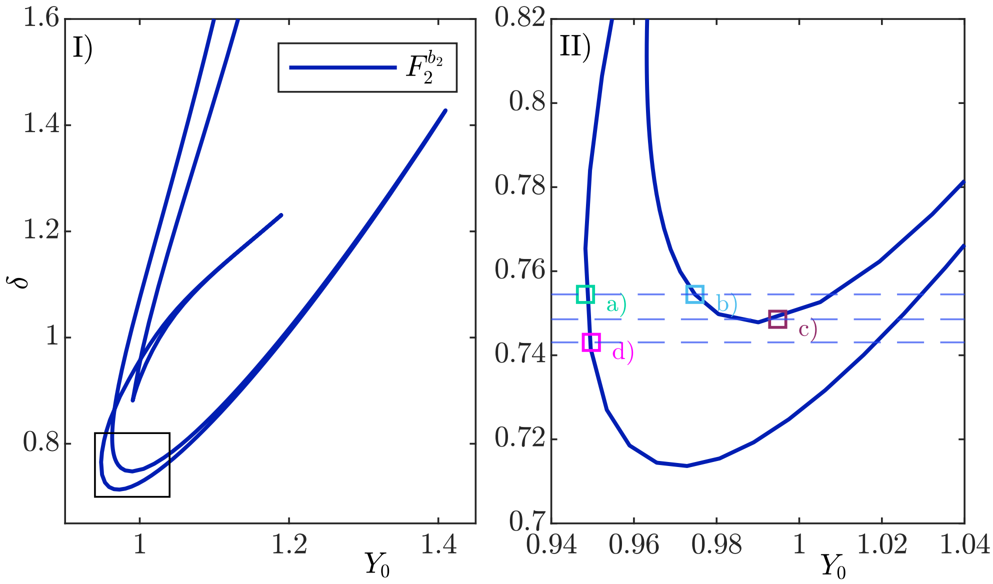

Figure 5.8: (I): Fold diagram gained from two-parameter continuation in Y_0 and δ, with a zoom-box in black marking the area of interest for one-parameter continuations with δ =const. (II): Zoom-in on the lower limit of fold existence consisting of two loops, as marked by the black square in panel (I). One-parameter continuations were started at squares a) - d). The resulting branches are depicted in Fig. 5.9. Parameters are (h, η, φ, τ)=(2, 0.682, π, 300).

mechanisms of formation and annihilation of the two main folds $F_1^{b_2}$ and $F_2^{b_2}$, as well as to track the evolution of branch $b_2^{3\tau}$ in $(Y_0 - \delta)-$space, one-parameter continuations in Y_0 with δ at fixed values were employed in the area marked by the black square in Fig. 5.8 (I), in which the lower limit of fold existence is located. Consequently, just as in Sec. 5.2.1, four points a) - d) were chosen as starting points along the inner and outer loop.

The resulting branches are depicted in Fig. 5.9 (I) - (IV). Here, it can be observed that two major branch types can be discerned.
Branch b) and c), depicted in Fig. 5.9 (II) and (III), are of simple structure made up solely from two folds, their structure mirroring that of the closed isola solutions, which have already been discussed in the prior section, as well as branch $b_1^{3\tau}$ introduced in Sec. 5.1. They belong to the inner loop of the fold diagram depicted in Fig. 5.8 (II).

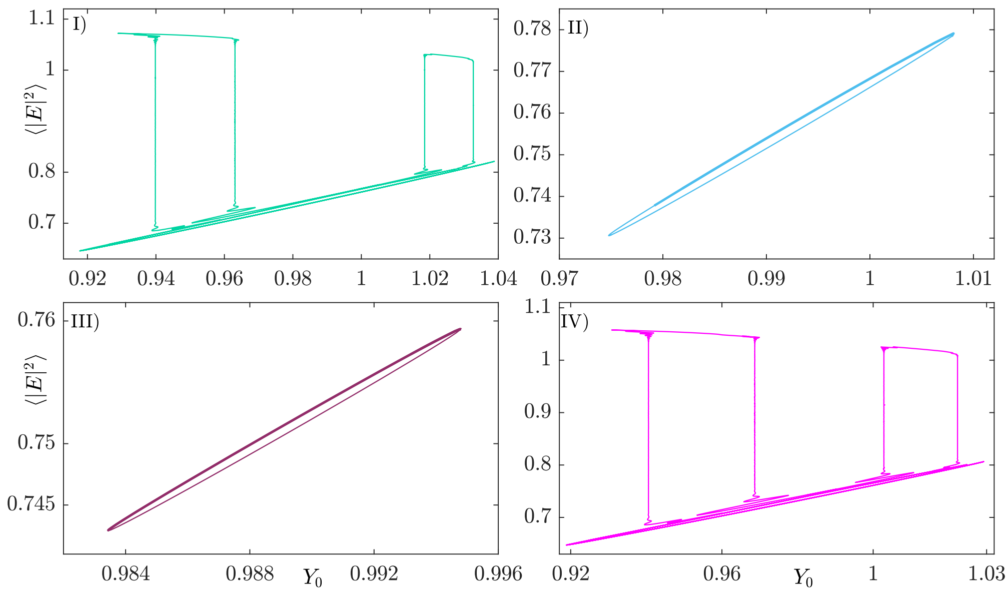

Figure 5.9: (I) - (IV): Branches gained from one-parameter continuations evaluated at squares a) - d) of matching color depicted in Fig. 5.8. Two types of branches can be distinguished. Branch b) and c) depicted in panels (II) and (III), which belong to the inner loop of fold existence, are closed isola solutions of simple structure, determined solely by two main folds. In contrast, branch a) and d) depicted in panel (I) and (IV) belong to the outer loop and are constituted by two type $b_2^{3\tau}$ branches connected at their base by a complex folding structure. Parameters are (h, η, φ, τ)=(2, 0.682, π, 300).

In contrast, branches a) and d) belonging to the outer loop feature a much more complicated structure. Alongside the two main folds $F_1^{b_2}$ and $F_2^{b_2}$, the base of branches a) and d) features a multitude of different folds connecting two branches, which each resemble branch $b_2^{3\tau}$ in their basic structure.
From the extent of branch a) and d), as depicted in Fig. 5.9 (I) and (III), it becomes evident that $F_1^{b_2}$ and $F_2^{b_2}$ can no longer be considered branch a)'s and d)'s main folding points, since they no longer define their widest extent in Y_0. For instance, the widest extent of branch a), as depicted in Fig. 5.9 (I), is approximately $Y_0 = 0.918$ to $Y_0 = 1.04$, while the fold diagram in Fig. 5.8 predicts the location of $F_1^{b_2}$ and $F_2^{b_2}$ for point a) at about $Y_0 = 0.95$ to $Y_0 = 1.03$ respectively. To analyze the relationship between branches a) - d) and to examine their evolution as the lower limit of fold existence is approached, all four branches were plotted together with the CW branch in black in Fig. 5.10 (II)

and (III). For reference, their starting points on the fold diagram, marked by squares of

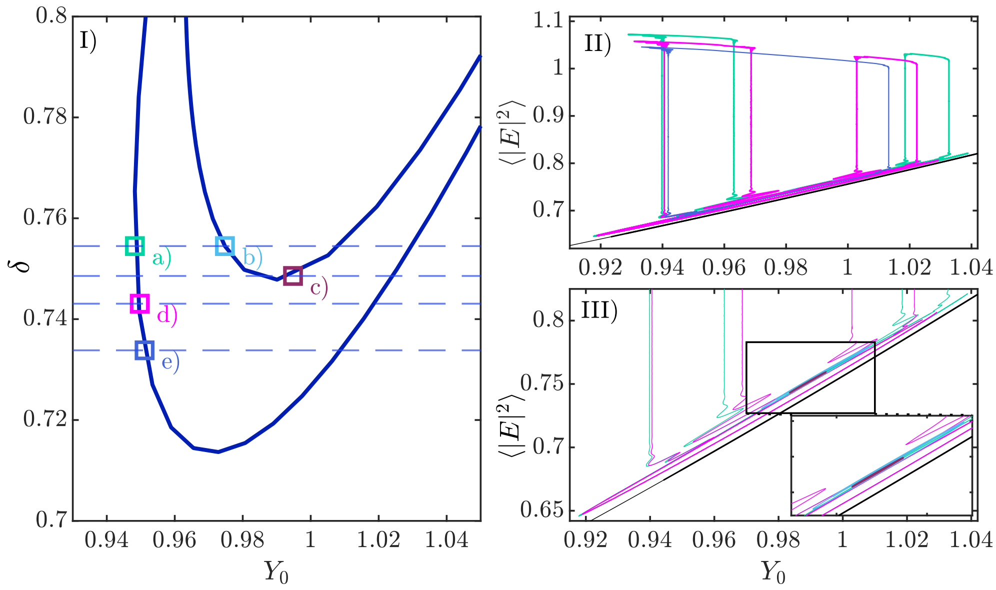

Figure 5.10: (I): Starting points for one-parameter continuations in Y_0 along the inner and outer loop of the lower limit of fold existence are marked by squares a) - e). (II): Branches a) - e), corresponding to the starting points of matching color depicted in panel I), are plotted together with the CW branch in black. In the zoom-box in panel (III), it can be observed that branches b) and c) are entirely contained within the structure of branches a), d) and e). For branches a) - e), no convergence to the CW branch can be observed. Parameters are (h, η, φ, τ)=(2, 0.682, π, 300).

matching colors, is depicted in panel (I) of the same figure. Since from Fig. 5.10 (II) and (III) it becomes immediately apparent, that branches a), d) and e) evolve independently from branch b) and c), their evolution as the lower limit of fold existence is approached, will be analyzed separately.

Hence in the following, first the evolution of the branches living on the outer loop, here exemplified by branch a), d) and e), will be examined. Then, the analysis will turn to the evolution of the branches with starting points on the inner loop, exemplified by branch b) and c).

To begin with, as displayed in Fig. 5.10 (II), a comparison of branch a) with branch d) illustrates, that with decreasing values for δ the branches functional structure is retained, while its overall extent decreases in size. This demonstrates, that although the width of branches a) and d) depends on a multitude of different folds, the branches as a whole follow the dynamic of $F_1^{b_2}$ and $F_2^{b_2}$ moving closer together, as δ is decreased. As can be seen in the zoom-in in Fig. 5.10 (III), going from branch a) to branch d) no significant convergence to the CW branch can be observed. Furthermore, from comparison of branch d) with branch e), it can be observed that the two branches of type $b_2^{3\tau}$, which make up the structure of branch d), have merged into a single branch of type $b_2^{3\tau}$, as exemplified by branch e). Regarding this transformation, the following observations can be made.

By direct comparison of the structure of branch a) and d) with branch e), it becomes evident that the surviving two Maxwell lines of branch e) correspond to the outer pair of Maxwell lines of branches a) and d). On the other hand, as visible in Fig. 5.10 (II) - (III) going from branch a) to branch d), the inner pair of Maxwell lines can be seen so steadily converge towards one another.

It can thus be hypothesized, that evolving from branch d) to e), the inner pair of Maxwell lines must have converged further and finally collided at some point, consequently vanishing from the branch. This leaves the outer pair of Maxwell lines to define the structure of branch e). Since the two main folds of branch a) and d), which can also be observed to converge in Fig. 5.10 (III), are no longer present in branch e), it can additionally be hypothesized that here we observe the same mechanism, which was encountered in the upper limit of fold existence for φ, as displayed in Fig. 5.5 (III), leading to the annihilation of folds in pairs of two, while a closed isola solution is left behind. To further investigate the evolution of branches belonging to the outer loop, as the lower limit of fold existence is approached, two more branches were calculated with starting points f)

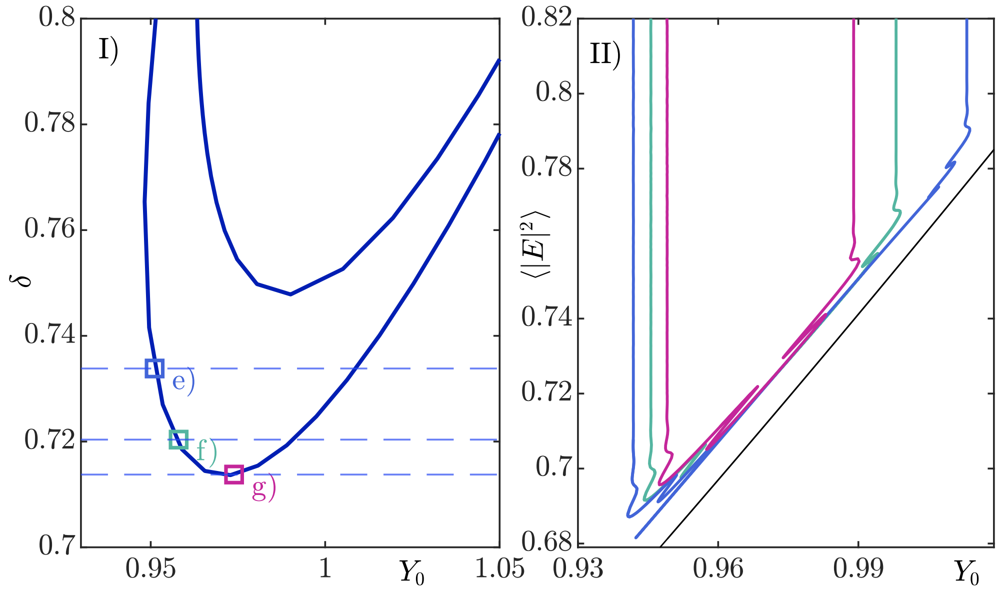

Figure 5.11: Evolution of branches e), f) and g) along the outer loop of fold existence approaching its lower limit. All three of them exhibit the structure known from branch $b_2^{3\tau}$. (II): Evolving from branch e) to g), the number of folds, which are part of base of the branches, can be observed to decrease pairwise. This behavior can be explicitly observed for the pair of folds described by the outer loop in panel (I). Correspondingly, at the base of branch g), an almost closed isola solution is visible. Evolving from branch e) to g), no convergence to the CW branch (black) can be observed. Parameters are (h, η, φ, τ)=(2, 0.682, π, 300).

and g), with g) being the closest to the turning point of the outer loop at approximately $\delta = 0.713$ and $Y_0 = 0.965$. Branches e), f) and g) are depicted in Fig. 5.11. Note that, since the interesting dynamics occur at the base of all three branches, the top of the branches was left out for better visibility. For reference, all three branches exhibit the known structure of branch $b_2^{3\tau}$.

From Fig. 5.11 the following conclusions can be drawn. First of all, between branch d) and e) a separation of the two type $b_2^{3\tau}$ branches, which branch d) consisted of, has occurred and the number of folds, which make up the base, have decreased significantly leading to an overall decrease in branch complexity. Furthermore, comparing branch e) to branch f) and branch f) to branch g) it can be observed, that the number of folds constituting the base of the branches, decreases pairwise, as they approach each other steadily. This behavior can be explicitly observed for the two main folds, whose convergence is described by the fold diagram in 5.11 (I). In branch g), which was calculated close to the turning point of the inner loop of fold existence, it can be observed that the two inner folds have almost collided. Accordingly, a nearly closed isola solution can be seen attached to the two folds. This is in perfect correspondence to the mechanism already observed in the upper limit of fold in φ displayed in Sec. 5.2.1 Fig. 5.5 (III).

Due to the similarities in structure, it is thus plausible to assume that each time a pair of folds collides a closed isola spanned by the remaining outer folds is left behind, exactly as observed in Fig. 5.5 (IV). Additionally, comparing branch e) to branch g) as depicted in Fig. 5.11 (II) no convergence to the CW branch in black can be observed. Instead, in agreement with the results from the upper limit of fold existence in φ, again an independent scenario of SW_3 branch formation and annihilation is encountered.

With the analysis of the evolution along the outer loop complete, now the evolution of branches along the inner loop is examined. For a better illustration of the branches evolution as the lower limit of the inner loop is approached, in addition to branches b) and c), another branch h) was calculated from one-parameter continuation, using a starting point positioned even closer to the lower limit of existence. All three branches are depicted in Fig. 5.12 (II).

As evident, going from branch b) to branch h) the pair of folds steadily converge, as predicted by the fold diagram in Fig. 5.12 (I). Branch h) retains the structure of branch b) and c) and is hence completely engulfed by both of them. Comparing branch c), f) and g) directly, again no convergence to the CW branch plotted in black can be observed. Since the functional structure of the branches b), c) and h) is determined solely by the two folds converging into one another, it can be argued that the extent of the branch belonging to the turning point in δ and Y_0 approaches zero. This again perfectly mirrors the behavior observed for the upper limit of fold existence in φ, as depicted in 5.5 (IV).

To sum up, in correspondence to the upper and lower limit of fold existence in φ, no bifurcation scenario connecting the SW_3 solution branches to the CW branch, or any other branch in that regard, was observed. Instead, an independent scenario of SW_3 branch formation and annihilation was encountered, which could be attributed to two

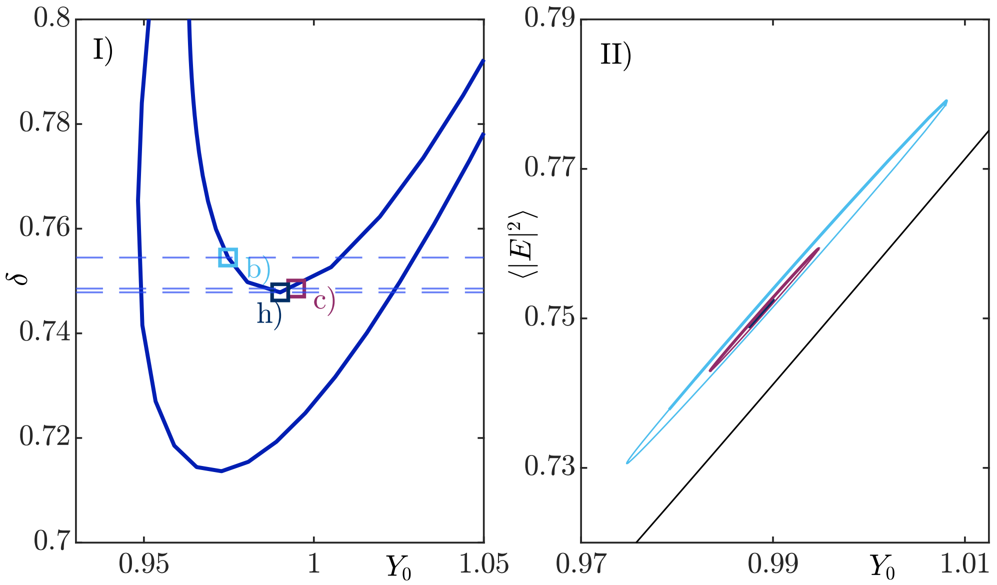

Figure 5.12: Evolution of closed isolas evaluated at exemplary points b), c) and h), as the lower limit of the inner loop of fold existence is approached. As can be seen in (II), going from branch b) to h) their structure defining pair of folds converges, as predicted by the fold diagram in (I). This causes a continuous decrease of the extent of the branches, while no convergence to the CW branch in black can be observed. Parameters are (h, η, φ, τ)=(2, 0.682, π, 300).

central mechanisms. As depicted in Fig. 5.10 and Fig. 5.11, the SW_3 branches corresponding to the outer loop of fold existence merge, leaving behind a single branch, that mirrors the known structure of $b_2^{3\tau}$.

Approaching the lower limit of fold existence along the outer loop, these branches can be observed to lose their folds consecutively caused by pairwise collisions of folds, which belong to the base of the branches. As this mirrors perfectly the behavior observed in the upper limit of fold existence in φ in Sec. 5.2.1, it is a natural hypothesis, that for each collision of folds a closed isola solution is generated, leaving behind a series of closed SW_3 isolas in the process. This constitutes the first mechanism of SW_3 branch formation.

The evolution of these closed SW_3 isola solutions constitutes the second mechanism, which was observed for both parameters φ and δ, as evident in Fig. 5.5 (IV) and Fig. 5.12 respectively. Since their evolution is determined solely by the pair of main folds, they were observed to vanish without making a connection to the CW branch of the corresponding parameter set, as their structure-determining pair of folds converges and consequently annihilates in parameter space.

5.2.3. Two-Parameter Continuations in η

Lastly, in Fig. 5.13 the fold diagram gained from two-parameter continuation in η and Y_0 is depicted. In direct comparison to the fold diagram gained from varying Y_0 together with δ (see Fig. 5.7), obvious similarities regarding the functional structure can be observed. To begin with, both share the same two-fold looping structure at the lower

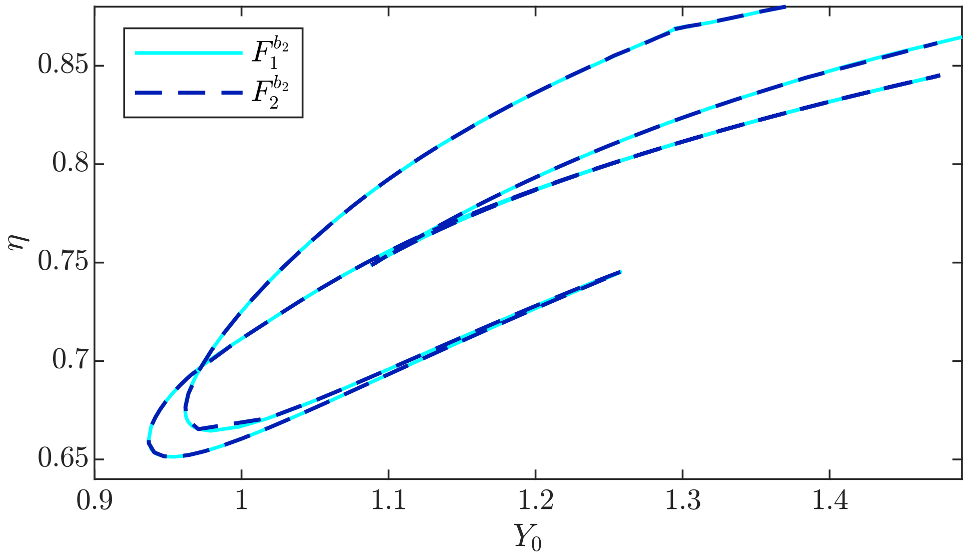

Figure 5.13: Fold diagram gained from two-parameter continuation of fold $F_1^{b_2}$ and fold $F_2^{b_2}$ in the system variables η and Y_0. As can be seen, the structure strongly resembles that of the fold diagram gained from varying δ. Both feature two looping structures in the lower limit of fold existence, as well as two hooks connecting to a crossover for $\eta \approx 0.7$ and $\eta \approx 0.75$. Parameters are $(\delta, h, \varphi, \tau)$=(0.8, 2, π, 300).

limit of existence for the folds $F_1^{b_2}$ and $F_2^{b_2}$, which can be located at injection values $Y_0 < 0.95$ and $\eta < 0.65$. Just like the fold diagram gained from varying δ, the looping structure feeds into a hook for increasing injection values Y_0. Furthermore, at $\eta \approx 0.7$ and $Y_0 \approx 0.97$ a crossover of both folds can be observed. In analogy to the fold diagram in δ, no upper boundary can be observed. Instead, the uppermost structure of the fold diagram steadily converges against one, which is to expected, since in contrast to the detuning δ, η can not assume values greater than one, because it can be interpreted as a refractive index. Based on the substantial similarities of the behavior of $F_1^{b_2}$ and $F_2^{b_2}$ in $(\delta - Y_0) -$ space, as well as in $(\eta - Y_0) -$ space, as displayed by the two fold diagrams depicted in Fig. 5.7 and Fig. 5.13 respectively, it can be hypothesized that the evolution of branches and the corresponding mechanisms are analogous for both parameters.
A more detailed analysis is out of the scope of this thesis, but could be conducted utilizing the same approach, which was chosen to analyze the behavior of the formation and annihilation of $F_1^{b_2}$ and $F_2^{b_2}$ in the parameters φ and δ.

6. Analysis of Subharmonic Solutions

This chapter concerns the analysis of the subharmonic branches, which constitute another type of SW branches, that are solutions to the KGTI system Eqs. (2.14) and (2.15). The subharmonic branches were observed by [Koc22] to bifurcate from the CW branch in a cascade of n Hopf bifurcations, consequently reconnecting with it by the same bifurcation scenario. Correspondingly, the n-th subharmonic SW branch was observed to correspond to a period of $T = \frac{2\tau}{2n-1}$. As visible in Fig. 4.3, all subharmonic solutions identified by [Koc22] were observed to be unstable for $n > 1$.
Expanding on the findings of [Koc22], in this section the results of the analysis of subharmonic solutions within the KGTI system for an additional two parameter sets will be presented. The central aim of this section will be to analyze these additional subharmonic solutions in terms of their stability and functional structure, as well as regarding their scenario of formation and annihilation. Consequently, a comparison to the subharmonic solutions identified by [Koc22] will be conducted.
All of the subharmonic branches presented in this section were gained by one-parameter continuation in Y_0. The Hopf bifurcation points along the CW branch, from which they can be observed to bifurcate, pose as starting points for the one-parameter continuations in Y_0 and were located by evaluation of the eigenvalue spectrum of the CW branch of the corresponding parameter set. This was done because the position of a Hopf bifurcation occurring along the CW branch is determined by two complex conjugated eigenvalues crossing the imaginary axis. As a consequence, the pair of eigenvalues suddenly turns real, allowing to pinpoint the location of a Hopf bifurcation along the CW branch, that gives rise to a periodic solution branch.
To begin with, subsequent to the parameter set examined by [Koc22], the first parameter set regarded in this thesis is constituted by a reduction in delay from $\tau = 300$ to $\tau = 100$. The resulting subharmonic branches, that can be found to exist within this modified parameter set $(\delta, h, \eta, \varphi, \tau) = (0.2,\ 2,\ 0.9,\ \pi,\ 100)$ are depicted together with their corresponding periods in Fig. 6.1. In agreement with the results of [Koc22], all four branches can be observed to bifurcate from the CW branch of this modified parameter set in a series of Hopf bifurcations at $Y_0 \approx 0.58$ consequently reconnecting with it in the vicinity of $Y_0 \approx 0.93$.
To begin with, the first periodic branch colored in blue corresponds to the highest possible period of $T = \frac{2\tau}{1} = 2\tau$ for the case of $n = 1$, instantiated by the first Hopf bifurcation. The three subsequent subharmonic branches can be observed to match the pattern of $T = \frac{2\tau}{2n-1}$ for $n = 2, 3, 4$ alike for the reduced delay of $\tau = 100$.
In comparison to the subharmonic branches observed by [Koc22], the functional structure of the subharmonic branches observable for the reduced delay of $\tau = 100$ is largely retained and with the exception of the branch for $n = 1$, all of the subharmonic branches can be observed to be unstable. As a notable difference to the subharmonic branches identified by [Koc22], it becomes evident that the snaking structure following the Hopf

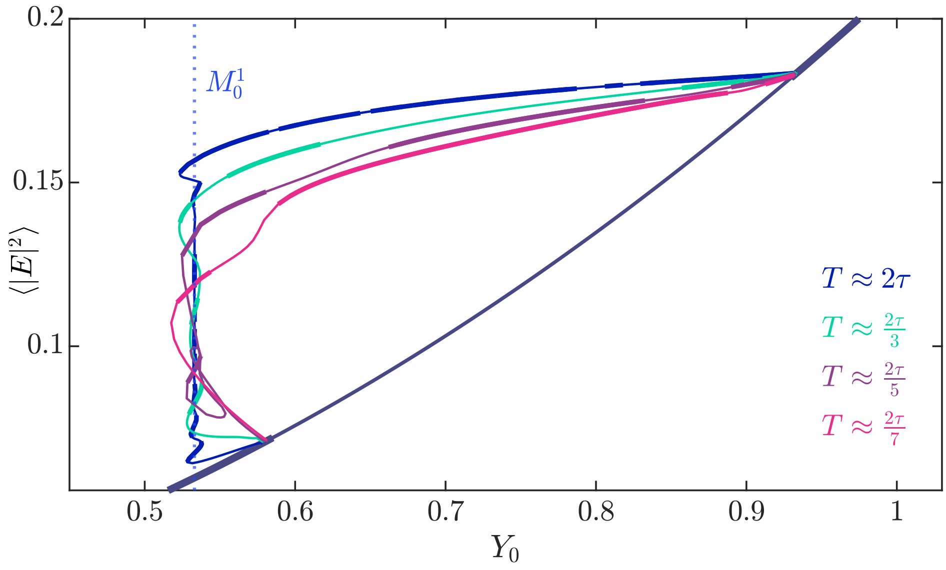

Figure 6.1: The first four subharmonic branches bifurcating from the CW branch (black) in a cascade of Hopf bifurcations at $Y_0 \approx 0.58$ consequently reconnecting with it at $Y_0 \approx 0.95$ in another cascade of Hopf bifurcations. Their corresponding periods plotted in lower right corner match the expected pattern of $T = \frac{2\tau}{2n-1}$. Parameters are $(\delta, h, \eta, \varphi, \tau)$= (0.2, 2, 0.9, π, 100).

bifurcation from the CW branch becomes more complicated in the case of the third subharmonic branch with $T = \frac{2\tau}{5}$, with numerous circular structures and crossing-overs. With the exception of this quality, the subharmonic branches identified within the parameter set $(\delta, h, \eta, \varphi, \tau)$ = (0.2, 2, 0.9, π, 100) thus mirror the subharmonic branches observed by [Koc22] in terms of stability, functional structure, as well as their scenario of formation and annihilation.

With the analysis of the subharmonic branches for the first parameter set concluded, a set of subharmonic solutions, which exhibit an entirely different functional structure, can be observed for the parameter set $(\delta, h, \eta, \varphi, \tau)$ = (0.5, 2, 0.75, 1.0472, 100). The first four subharmonic branches corresponding to this new parameter set are plotted in Fig. 6.2. In agreement with the findings for the two prior parameter sets, the first four subharmonic branches can be observed to consecutively bifurcate from the CW branch in a series of Hopf bifurcations, as visible in the zoom-in Fig. 6.2, consequently reconnecting with the CW branch in another series of Hopf bifurcations.

They thus mirror perfectly the mechanism of formation, as well as annihilation of the subharmonics branches observed by [Koc22]. Their respective periods plotted in the bottom right of Fig. 6.2 again match the expected pattern of $T = \frac{2\tau}{2n-1}$ for the n-th subharmonic branch.

However, in contrast to the subharmonic branches from the two prior parameter sets, key differences can be discerned, that regard the functional structure, as well as the stability of the subharmonic branches found within this parameter set. First of all, regarding

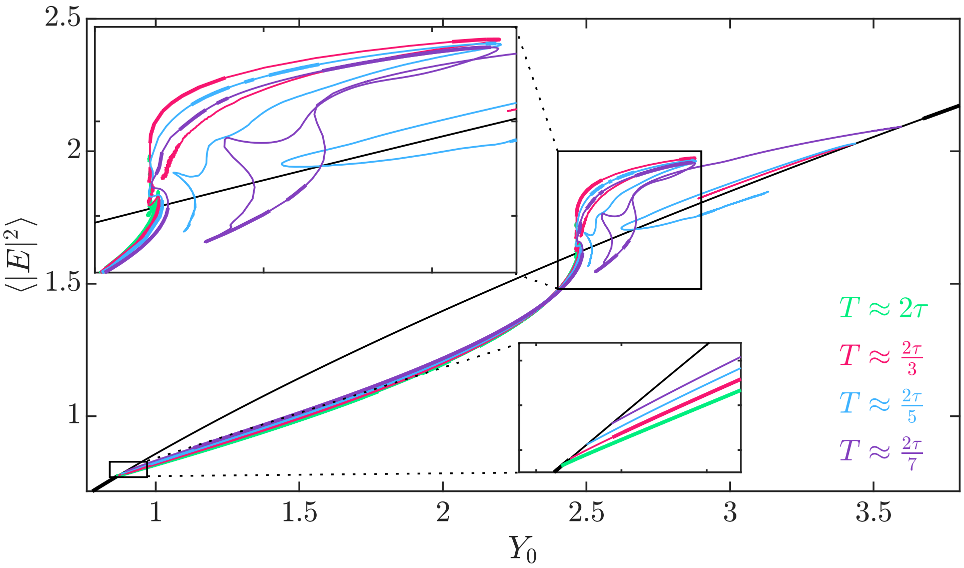

Figure 6.2: The first four subharmonic branches bifurcating from the CW branch (black) in a cascade of Hopf bifurcations at $Y_0 \approx 0.99$, as explicitly visible in the zoom-box, consequently reconnecting with it at $Y_0 \approx 3.5$ in another cascade of Hopf bifurcations. Their corresponding periods plotted in the lower right corner match the expected pattern of $T = \frac{2\tau}{2n-1}$. All four branches exhibit complicated snaking behavior in the center section at $Y_0 \approx 2.5$, through which only the fourth subharmonic branch could be continuated completely. Parameters are $(\delta, h, \eta, \varphi, \tau) = (0.5,\ 2,\ 0.75,\ 1.0472,\ 100)$.

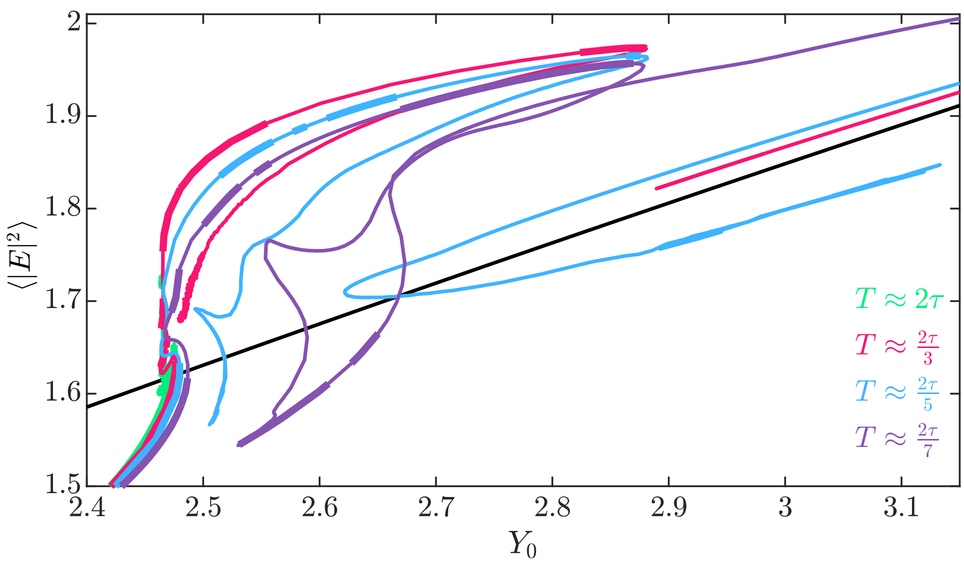

Figure 6.3: Zoom-in on the center section of the first four subharmonic branches, which exhibits a complex fold bifurcation scenario with sharp turns, as well as crossing-overs. Parameters are $(\delta, h, \eta, \varphi, \tau) = (0.5,\ 2,\ 0.75,\ 1.0472,\ 100)$.

their differences in structure, they can be observed to exist for a much wider interval of injection values, bifurcating at about $Y_0 \approx 0.9$ and reconnecting with the CW branch in the vicinity of $Y_0 \approx 3.5$. In the first and last section of the subharmonic branches, the corresponding periodic solutions can be observed to develop without undergoing any bifurcations. However, as visible in Fig. 6.3 between $Y_0 \approx 2.4$ and $Y_0 \approx 2.9$ they exhibit a highly complex behavior consisting of multiple folding structures as well as crossing-overs. This behavior distinguishes them clearly from the subharmonic branches observable within the parameter set of [Koc22], as well as the parameter set considered in the beginning of this chapter.

Directly relating to this, only the subharmonic branches with a period of $T = \frac{2\tau}{7}$ and smaller could be explicitly tracked through their complex middle section by means of one-parameter continuation. To show that the first three subharmonic branches with $T = 2\tau$, $T = \frac{2\tau}{3}$ and $T = \frac{2\tau}{5}$ actually reconnect to the CW branch, the corresponding Hopf bifurcation points were located in the vicinity of $Y_0 = 3.5$ by evaluation of the characteristic eigenvalue spectrum of the CW branch. Once again, one-parameter continuations were started at the bifurcation points tracking the path of the branches as far as possible into the area of complex snaking in reverse.

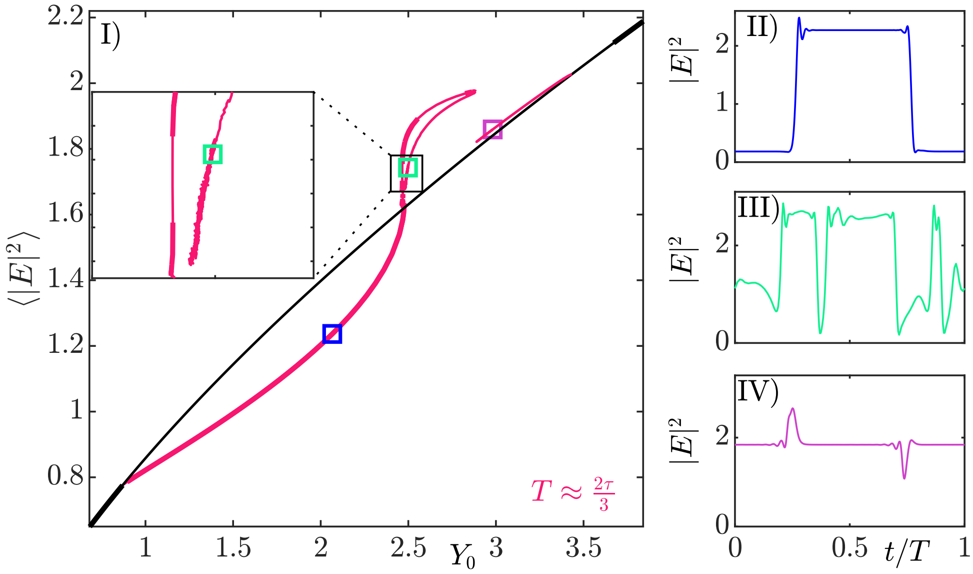

Figure 6.4: (I): Plot of the second subharmonic branch in light-red with three exemplary profiles depicted in panels (II)-(IV) and a zoom-in on the area, where it became increasingly difficult to continuate the branch with DDE-BIFTOOL. In panel (II), a fully developed two-plateau SW with a period of $T \approx \frac{2\tau}{3}$ can be observed. (III): Pulses of different amplitudes can be observed to interfere with the underlying SW solution from panel (I) resulting in a drift bifurcation-like behavior. (IV): An alternating pulse solution is visible retaining the period of $T \approx \frac{2\tau}{3}$. Parameters are $(\delta, h, \eta, \varphi, \tau) = (0.5,\ 2,\ 0.75,\ 1.0472,\ 100)$.

As will now be shown, the complex structure of the subharmonic branches located within this parameter set corresponds to a much more intricate evolution of profiles along the branches. Furthermore, the analysis of profiles can also explain, why it is difficult to follow the first three subharmonic branches through their complex center section with DDE-BIFTOOL.

Consider therefore Fig. 6.4, in which the second subharmonic branch is plotted in light red together with three profiles evaluated at characteristic points marked by squares of matching color. To begin with, as visible in Fig. 6.4 (II), a fully developed two-plateau SW profile can be seen to have developed from the Hopf bifurcation point along the vertical section of the branch. This constitutes the standard mechanism of SW formation, that has already been observed for the subharmonics found within the parameter set of [Koc22], as well as the modified parameter set considered in the beginning of this chapter. With a period of approximately $T = \frac{2\tau}{3}$, the resulting SW profile is again in agreement with the expected pattern of $T = \frac{2\tau}{2n-1}$ for the second subharmonic with $n = 2$.

However, approaching the complex center section of the second subharmonic branch, where the continuation software struggled to follow its pathway, it becomes evident that in this area small and large amplitude pulses deform the underlying SW solution created by the series of fold bifurcations, as demonstrated by the exemplary profile depicted in Fig. 6.4 (II). The observable behavior is similar to that of a drift bifurcation with a pulse emerging at one end of a plateau consequently drifting to the other end. Since the movement of these pulses on top of the SW solution leave the measure $\langle |E|^2 \rangle$ of the profiles nearly unchanged, the continuation software DDE-BIFTOOL struggles to correctly calculate the next step in parameter space to a given profile, as the branch progresses through this section exhibiting drift bifurcation-like behavior. Since the continuation software is nonetheless forced to take a finite step as a guess for the location of the adjacent solution in parameter space, this results in a discontinuous jitter observable explicitly in Fig. 6.3 and in the zoom-in in Fig. 6.4 (I).

The same problem arises analogously for the first and third harmonic branch, as made evident by the same jitter observable in Fig. 6.3. Again, this is a direct consequence of the drift bifurcation-like behavior observable within the center section of the first three subharmonics.

Finally, the profile depicted in Fig. 6.4 (IV) demonstrates, that after transgressing the complex center section the solution has transformed from a two-plateau SW solution into an alternating pulse solution of the same period. This behavior marks another characteristic, that clearly differentiates the subharmonic solutions analyzed within this parameter set from the subharmonics considered by [Koc22] as well as the subharmonics analyzed in the beginning of this chapter. As will be seen, the transformation from a SW solution to a pulse solution of the same or increased periodicity is also observable for subharmonic branches of higher order, which will be analyzed next. In contrast to

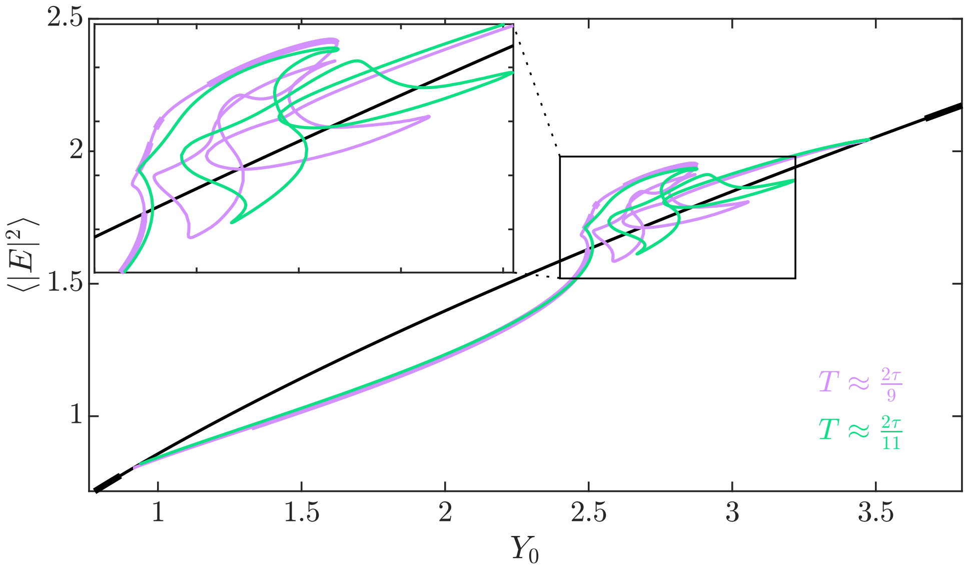

Figure 6.5: The fifth and sixth subharmonic branches with their corresponding periods in the bottom right corner, bifurcating from the CW branch (black) in two Hopf bifurcations, consequently reconnecting with the CW branch in the same bifurcation scenario. In the zoom-in, the center section of both branches is visible, which exhibits numerous fold bifurcations resulting in sharp turns and numerous crossing-overs. Parameters are $(\delta, h, \eta, \varphi, \tau) = (0.5,\ 2,\ 0.75,\ 1.0472,\ 100)$.

the first three subharmonic branches of this parameter set, the subharmonic branches corresponding to periods of $T = \frac{2\tau}{7}$ and higher can be tracked completely by means of one-parameter continuation, uncovering their complex snaking behavior in the center section, as explicitly plotted for the subharmonic branches with a period of $T = \frac{2\tau}{7}$ in Fig. 6.3 and the two subsequent subharmonic branches with a period of $T = \frac{2\tau}{9}$ and $T = \frac{2\tau}{11}$ in Fig. 6.5. Although not explicitly plotted, a complete continuation of the subharmonic branches in this parameter set up until order $n = 8$ corresponding to a period of $T = \frac{2\tau}{15} \approx 13.3$ was achieved within the scope of this thesis.

In Fig. 6.6, the fifth subharmonic branch with a period of $T = \frac{2\tau}{9}$ is depicted in violet together with three characteristic profiles in panels (II) - (IV). Again, it can be observed that from the Hopf bifurcation a fully developed two-plateau SW solution exemplified by Fig. 6.6 profile (II) with a period of approximately $T = \frac{2\tau}{9}$ can be seen to develop, as the section running parallel to the unstable CW branch is progressed. The corresponding SW solution exists up until the initial hooking structure at approximately $Y_0 = 2.5$.

Interestingly, as demonstrated by Fig. 6.6 (III), it can be observed that the two-plateau SW turns into a periodic solution with an increased periodicity consisting of five pulses as the complex snaking section is transgressed. Indeed, the evolution of two-plateau SW solutions into pulse solutions via transgression of the center section of the subharmonics was observed for all subharmonic branches up until $n = 8$, with periodic solutions

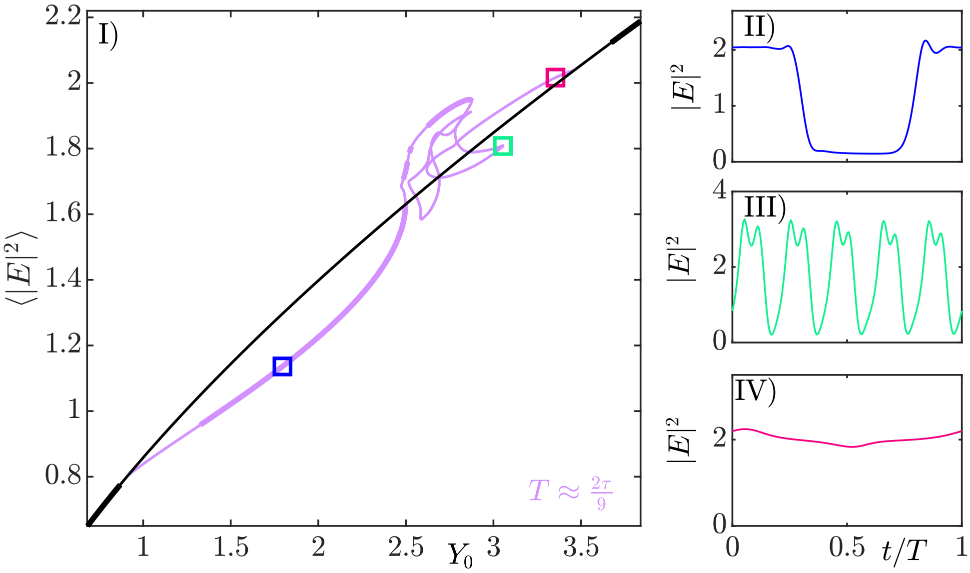

Figure 6.6: (I): The fifth subharmonic branch plotted in violet with three exemplary profiles plotted in panels (II) - (IV). (II): A fully developed SW profile with a period of $T \approx \frac{2\tau}{9}$ can be observed. In panel (III), a profile consisting of five pulses is visible. Relative to the SW profile in panel (II), its periodicity has increased approximately by a factor of five. (IV): The pulse solution from panel (III) can be observed to have almost completely evolved back to the the CW solution with an amplitude of $|E|^2 \approx 2$. Parameters are $(\delta, h, \eta, \varphi, \tau)$ = (0.5, 2, 0.75, 1.0472, 100).

consisting of two alternating pulses in the case of the second subharmonic, three pulses in the case of the subharmonic branches with $n = 8$, $n = 7$ and $n = 4$, five pulses in the case of $n = 6$ and $n = 5$ or even eleven pulses in the case of $n = 3$. Due to the increase in periodicity, theses solutions can be regarded as subharmonic solutions to the subharmonic solutions encountered in this parameter set.

Because of the transition of periodicity within the center section of the subharmonics, it becomes evident that here we observe a reconnection of subharmonic branches of different order with one another. Finally, in Fig. 6.6 (IV) the pulse solution of increased periodicity can be observed to steadily evolve back to a CW solution with an amplitude of $|E|^2 \approx 2$, as the branch closes in on the Hopf bifurcation point, where it finally merges with the CW branch. For reference, the CW amplitude value of $|E|^2 \approx 2$ coincides with the value for the upper plateau of the SW solution in Fig. 6.6 panel (II).

Finally, regarding the stability of the subharmonic branches, it can be determined that the branches with a period of $T = \frac{2\tau}{5}$ and $T = \frac{2\tau}{7}$ depicted in Fig. 6.2, as well as the branches with a period of $T = \frac{2\tau}{9}$ and $T = \frac{2\tau}{11}$ depicted in Fig. 6.5 can be observed to be unstable matching the observations from the prior two parameter sets for the instability of subharmonic branches of order $n > 1$. It is most notable however, that the second subharmonic branch corresponding to a period of $T = \frac{2\tau}{3}$ can actually observed to be stable until it reaches the section of complex folding, as visible in Fig. 6.4 (I). This demonstrates that stable subharmonic branches indeed exist within the KGTI system. To summarize, regarding the subharmonic solutions that were shown to exist within the two additional parameter sets evaluated within this chapter, the following conclusions can be drawn.

First of all, it was demonstrated that for both parameter sets the subharmonic branches can be observed to bifurcate from the CW branch in a cascade of Hopf bifurcations consequently reconnecting with the CW branch in yet another cascade of Hopf bifurcation. The scenario of formation as well as annihilation thus matches the scenario already described by [Koc22]. Regarding the functional structure of the subharmonics considered within this chapter, the following observations could be made. Concerning the subharmonic branches found within the first parameter set evaluated within this chapter, it became evident that their structure largely mirrored the subharmonic branches analyzed by [Koc22], with the exception of the third subharmonic branch exhibiting a slightly more complex structure.

Regarding the subharmonic branches identified within the second parameter set however, it was shown that they exhibit a completely disparate structure, bridging a much wider interval in Y_0 and featuring a complex fold bifurcation scenario in their center section with numerous sharp turns and crossing-overs. In direct correspondence to the heavily altered branch structure, from the evolution of profiles it was additionally shown, that the subharmonic branches from the second parameter set exhibit behavior that could hint to the occurrence of drift bifurcations along the center section of the branches.

Building upon this, it was then shown, that the two-plateau SWs emerging from the Hopf bifurcations in the beginning section of the subharmonic branches could be observed to transform into pulse solutions with an altered periodicity, as the branches center section is traversed. This behavior demonstrates, that here a reconnection of subharmonic branches of different order occurs.

Finally, it was also observed, that at least one subharmonic branch from parameter set two with a period of $T = \frac{2\tau}{3}$ turned out to be stable. All of these features are unique to the subharmonic solutions analyzed within the second parameter set and could not be observed for the parameter set analyzed by [Koc22], as well as for the parameter set evaluated in the beginning of this chapter. The observation of these unique characteristics marks the central result of this chapter.

7. Conclusion and Outlook

In this thesis the dynamics of square-wave solutions in time-delayed Kerr micro-cavities at the example of an injected Kerr Gires-Tournois interferometer in the long delay limit were examined. Expanding on the comprehensive description of period 2τ-SW solutions by [Koc+22], the primary goal of the first part of this thesis was the analysis of period 3τ-SW solutions, focusing both on their mechanism of formation and annihilation, as well as their corresponding evolution in parameter space. Regarding their scenario of formation, both a bifurcation scenario from the CW branch, which was observed explicitly for the case of 2τ-periodic SW solutions by [Koc22], as well as an independent scenario of formation were considered. The analysis was accomplished by a combination of direct numerical simulations, as well as numerical path-continuation utilizing the DDE-BIFTOOL package based on an implementation of the system as a DAE model in Matlab.

To begin with, three isolated SW_3 solution branches $b_1^{3\tau}$, $b_2^{3\tau}$ and $b_3^{3\tau}$ were presented and analyzed with special regards to the dynamics of SW profiles conducting a round trip along the branches. By a comparison of branch $b_3^{3\tau}$ with branch $b_2^{3\tau}$, it was shown that they feature the same structure and equivalent dynamics for SW profiles. Since $b_3^{3\tau}$ was gained through variation of phase feedback φ, this demonstrates that both the structure of the archetype of branch $b_2^{3\tau}$ as well as corresponding SW dynamics are not exclusively found through variation of injection Y_0, but can also be observed within the KGTI system through the variation of phase feedback φ.

Since all three branches were observed to be isolated, their evolution in parameter space as well as their scenario of formation was subsequently examined by means of two-parameter continuation in the injection Y_0, together with a variation of phase feedback φ, detuning δ and coupling strength η respectively. The points selected for two-parameter continuation were the two main folding points. Posing as structure defining bifurcations, tracking their evolution in parameter space constitutes an effective way of tracking the functional structure of the branch as a whole.

From the resulting fold diagrams it was shown, that SW_3 solutions can be observed for a wide range of parameter values in φ, δ and η within the KGTI system. In particular, these findings illustrate that SW_3 solutions are not exclusively found for $\varphi = \pi$, but for a wide range of phase feedback values, expanding on the results of [Koc22].

Subsequently, one-parameter continuations were employed in areas of interest throughout the fold diagrams, predominantly constituted by the upper and lower limit of existence of the two main folds.

Both in the upper- as well as in the lower limit of existence in the parameters φ and δ, no bifurcation scenario involving the connection of the SW_3 branches to the CW branch of the corresponding parameter set was observed, which would have allowed to attribute he formation of SW_3 solutions to the known mechanism of SW_2 solutions within the KGTI system. Instead, the resulting SW_3 solution branches remained isolated throughout the

analysis, constituting an independent scenario of formation within the KGTI system. Based on this, approaching the corresponding limits of fold existence, two central mechanisms of SW_3 branch formation and annihilation could be observed.
Firstly, for SW_3 branches of type $b_2^{3\tau}$ it was observed, that pairs of folds belonging to the base of the branch collide and consequently annihilate. This causes a separation of a closed isola solution spanned by a single pair of folds from the main branch, which was shown to continue existing independently. These closed isola solutions perfectly mirrored the structure of branch $b_1^{3\tau}$. Taking into account the independent evolution of the remaining main branch, it was then argued, that this mechanism is likely to repeat itself and is thus to be regarded as a genuine and methodical feature of SW_3 formation within the KGTI system.
In perfect agreement with this hypothesis, by examination of the outer loop of the lower limit of fold existence in δ, again a branch of type $b_2^{3\tau}$ was observed to lose a series of folds consecutively in pairs of two. For the pair of folds described by the fold diagram at hand, an almost closed isola solution, ready for separation from the main branch, was explicitly observed. Taken together it was concluded, that the collision and consequent annihilation of folds in pairs of two from branches of type $b_2^{3\tau}$ causing the formation of a series of independent isola solutions can be regarded as a genuine and methodical feature of SW_3 branch formation within the KGTI system.
Correspondingly, the independent evolution of these closed SW_3 isola solutions constitutes the second mechanism of SW_3 branch formation and annihilation, observed within the scope of this thesis. Both in the upper limit in φ as well as in the lower limit in δ, isola solutions of type $b_1^{3\tau}$ were observed to evolve exclusively according to the behavior of convergence of the pair of folds constituting their extent in parameter space. Approaching the limit of fold existence, they were observed to vanish independently from the CW branch of the corresponding parameter set, or any other type of branch in that regard, as their structure determining pair of folds converged and consequently annihilated in parameter space.
While the second mechanism describes the annihilation of closed SW_3 isola solutions, a possible final state of type $b_2^{3\tau}$ branches was observed in the lower limit of fold existence in φ. Here, a branch was identified, which had lost all of the folds constituting its base, presumably due to the annihilation of folds in pairs of two, leading to a complete disappearance of the collapsed snaking structure on both sides of the branch.
All in all, in this thesis two central mechanisms describing the evolution as well as formation and annihilation of SW_3 solutions within the KGTI system have been explicated. In contrast to the SW_2 solutions, which were observed to bifurcate from the CW branch of the corresponding parameter set, the two mechanisms observed for the case of the SW_3 solutions describe an independent scenario of SW branch formation and annihilation in parameter space. In a grander scheme of things, taken together the two mechanisms also explain the structural relationship between SW_3 branches of type $b_1^{3\tau}$ and branches of type $b_2^{3\tau}$ linking them together in a conjoint bifurcation scenario explaining why the

archetype of these two type of branches can be methodically observed within the KGTI system. While these central questions have been answered within the extent of this thesis, further investigations can be suggested based on the results of this thesis. This is partly due to limitations taken to maintain the extent of this thesis, which will be discussed in the following.

First of all, the two-parameter continuations focused solely on the two main folds from the base of branch $b_2^{3\tau}$. This methodology however, can be largely justified by the results gained from this thesis. As demonstrated by the first genuine mechanism of SW_3 branch formation, choosing any other fold from the base of a SW_3 branch of type $b_2^{3\tau}$ would very likely lead to the observation of the same results, since the first mechanism was observed to concern not only the two main folds, but every pair of folds of the base of the branches of type $b_2^{3\tau}$. This also validates the choice to limit the scope of this thesis to fold continuations of branch $b_2^{3\tau}$, instead of including fold continuations for branch $b_1^{3\tau}$ and/or $b_3^{3\tau}$ as well. Since all three branches can be attributed to two types, and these two types were demonstrated to be connected by a single type of bifurcation scenario, as explicated by the first mechanism described above, it can be plausibly hypothesized that fold continuations starting with different branches of type $b_1^{3\tau}$ and type $b_2^{3\tau}$ would likely lead to the same two mechanisms observed within this thesis. This hypothesis could of course be explicitly proven by continuations of folds from the base of different SW_3 branches of type $b_1^{3\tau}$ and $b_2^{3\tau}$. However, entirely new types of SW_3 branches in the form of two type $b_2^{3\tau}$ branches connected at their base by a complicated folding structure, as observed in the lower limit in δ, were encountered as well in this thesis. The analysis of their evolution in parameter space can thus be regarded as promising for further studies. Additionally, in the case of the fold diagram in δ, only the lower limit of fold existence was examined extensively. Since the fold diagram features several hooks and crossovers, which too can signify fundamental changes in branch structure, additional mechanisms of SW_3 branch formation and annihilation could potentially be observed in this section of fold existence as well. These areas could thus be examined by future studies by the same methodology employed in this thesis.

Furthermore, an explicit analysis of the fold diagram gained from varying the feedback strength η could confirm, whether the same mechanisms of SW_3 branch formation are encountered in η, as observed for the case of φ and δ. This was already suggested by strong analogies in structure of the corresponding fold diagrams in both parameters. Subsequent results could also be gained by continuations in the remaining system parameters left unexamined in this thesis.

Last but not least, as suggested by [Koc22] an analytical description of SW_3 solutions within the KGTI system might be possible, which was not considered within the scope of this thesis. Further research focusing on an analytical description of SW_3 solutions could thus be conducted and subsequently compared with the results gained in this thesis.

Finally, in the second part of this thesis another type of SW solutions, the subharmonic solution branches were analyzed in detail, once again by employing a combination of

one-parameter continuations and direct numerical simulations. Building on the results of [Koc22], subharmonic solution branches for an additional two parameter sets were evaluated. The central aim was to analyze their scenario of formation as well as annihilation, their functional structure and correspondingly the evolution of SW profiles along the respective branches and finally their stability.
Regarding their scenario of formation and annihilation, it was shown that they bifurcate from the CW branch of the respective parameter set in a cascade of Hopf bifurcation consequently reconnecting with it in another cascade of Hopf bifurcations consistent with the results of [Koc22]. Regarding their structure, it was observed that the subharmonic branches found within the first parameter set largely mirrored those analyzed by [Koc22], except for the third branch, which exhibited a slightly more complex structure. However, the subharmonic branches analyzed within the second parameter set displayed a completely different structure, spanning a much wider interval in Y_0 and featuring a complex fold bifurcation scenario with numerous sharp turns and crossovers in the center section.
Furthermore, regarding the evolution of profiles along the center section, drift bifurcation-like behavior was observed, marked by the formation of a pulse at one end of the SW plateau, consequently drifting to the other side. Additionally, it was shown that the two-plateau SWs emerging from the Hopf bifurcations in the initial section of the subharmonic branches, transform into pulse solutions with constant or altered periodicity as the subharmonic branches center section is traversed. This behavior indicates a reconnection of subharmonic branches of different orders. Finally, at least one subharmonic branch from the second parameter set with a period of $T = \frac{2\tau}{3}$ was determined to be stable. These features are unique to the subharmonic solutions of the second parameter set and were not observed in either the parameter set analyzed by [Koc22] or the modified parameter set evaluated in the beginning of chapter 6. Based on the results of the second part of this thesis, subsequent studies could regard the following aspects.
First of all, since the scope of this thesis was limited to the order of $n = 8$ for the subharmonics belonging to the second parameter set, further studies could regard even higher order subharmonics, as for instance to analyze their stability and whether they retain the complex structure and interrelated dynamics observed within their center section. Analyzing their stability could pose especially promising, since the stability of the second subharmonic branch with a period of $T = \frac{2\tau}{3}$ demonstrates, that stable subharmonic branches do exist within the KGTI system. Secondly, the drift bifurcation-like behavior encountered in the center section of the first three subharmonic branches of the second parameter set could be examined in detail, aiming for instance to identify whether the dynamics of pulses traveling through the SW profiles are caused by genuine drift bifurcations or are governed by a different mechanism. Last but not least, the interconnection of subharmonic branches of different order could be analyzed in detail, aiming to identify the underlying mechanisms and to identify potential patterns in the shift in periodicity, which is associated with the transformation from SW to pulse solution.

A. References

[ELR02] K. Engelborghs, T. Luzyanina, and D. Roose. “Numerical bifurcation analysis of delay differential equations using DDE-BIFTOOL”. In: *ACM Trans. Math. Softw.* 28.1 (2002), pp. 1–21. ISSN: 0098-3500. DOI: 10.1145/513001.513002. URL: https://doi.org/10.1145/513001.513002.

[Ern08] T. Erneux. *Applied Delay Differential Equations.* Dordrecht: Springer, 2008.

[Gav+06] A. Gavrielides et al. “Square-wave self-modulation in diode lasers with polarization-rotated optical feedback”. In: *Opt. Lett.* 31.13 (2006), pp. 2006–2008. DOI: 10.1364/OL.31.002006. URL: https://opg.optica.org/ol/abstract.cfm?URI=ol-31-13-2006.

[GT64] F. Gires and P. Tournois. “Interferometre utilisable pour la compression d’impulsions lumineuses modulees en frequence”. In: *C. R. Acad. Sci. Paris* 258 (1964), pp. 6112–6115.

[HGJ21] D. Hessel, S. V. Gurevich, and J. Javaloyes. “Wiggling instabilities of temporal localized states in passively mode-locked vertical external-cavity surface-emitting lasers”. In: *Opt. Lett.* 46.10 (2021), pp. 2557–2560. DOI: 10.1364/OL.428182. URL: https://opg.optica.org/ol/abstract.cfm?URI=ol-46-10-2557.

[Ike79] K. Ikeda. “Multiple-valued stationary state and its instability of the transmitted light by a ring cavity system”. In: *Optics Communications* 30.2 (1979), pp. 257–261. ISSN: 0030-4018. DOI: https://doi.org/10.1016/0030-4018(79)90090-7. URL: https://www.sciencedirect.com/science/article/pii/0030401879900907.

[JAH15] J. Javaloyes, T. Ackemann, and A. Hurtado. “Arrest of Domain Coarsening via Antiperiodic Regimes in Delay Systems”. In: *Phys. Rev. Lett.* 115 (20 2015), p. 203901. DOI: 10.1103/PhysRevLett.115.203901. URL: https://link.aps.org/doi/10.1103/PhysRevLett.115.203901.

[KAM10] A. M. Kaplan, G. P. Agrawal, and D. N. Maywar. “Optical Square-Wave Clock Generation Based on an All-Optical Flip-Flop”. In: *IEEE Photonics Technology Letters* 22 (7 2010). DOI: 10.1109/LPT.2010.2040997. URL: https://ieeexplore.ieee.org/document/5404908.

[KKP17] A. Keane, B. Krauskopf, and C. M. Postlethwaite. “Climate models with delay differential equations”. In: *Chaos: An Interdisciplinary Journal of Nonlinear Science* 27 (Nov. 2017), p. 114309. DOI: 10.1063/1.5006923.

[Koc22] E. R. Koch. “Square-waves and pulsating dynamics in time-delayed active micro cavities”. MA thesis. Universität Münster, 2022.

[Koc+22] E. R. Koch et al. “Square-wave generation in vertical external-cavity Kerr-Gires-Tournois interferometers”. In: *Opt. Lett.* 47.17 (2022), pp. 4343–4346. DOI: 10.1364/OL.468236. URL: http://opg.optica.org/ol/abstract.cfm?URI=ol-47-17-4343.

[Li+16] S.-S. Li et al. “Square-wave oscillations in a semiconductor ring laser subject to counter-directional delayed mutual feedback”. In: *Opt. Lett.* 41.4 (2016), pp. 812–815. DOI: 10.1364/OL.41.000812. URL: https://opg.optica.org/ol/abstract.cfm?URI=ol-41-4-812.

[LK80] R. Lang and K. Kobayashi. “External optical feedback effects on semiconductor injection laser properties”. In: *IEEE Journal of Quantum Electronics* 16.3 (1980), pp. 347–355. DOI: 10.1109/JQE.1980.1070479.

[MB05] J. Mulet and S. Balle. “Mode-locking dynamics in electrically driven vertical-external-cavity surface-emitting lasers”. In: *IEEE Journal of Quantum Electronics* 41.9 (2005), pp. 1148–1156. DOI: 10.1109/JQE.2005.853355.

[Oro+09] G. Orosz et al. “Exciting traffic jams: Nonlinear phenomena behind traffic jam formation on highways”. In: *Phys. Rev. E* 80 (4 2009), p. 046205. DOI: 10.1103/PhysRevE.80.046205. URL: https://link.aps.org/doi/10.1103/PhysRevE.80.046205.

[Sch+19a] C. Schelte et al. “Third Order Dispersion in Time-Delayed Systems”. In: *Phys. Rev. Lett.* 123 (4 2019), p. 043902. DOI: 10.1103/PhysRevLett.123.043902. URL: https://link.aps.org/doi/10.1103/PhysRevLett.123.043902.

[Sch+19b] C. Schelte et al. “Tunable Kerr frequency combs and temporal localized states in time-delayed Gires-Tournois interferometers”. In: *Opt. Lett.* 44.20 (2019), pp. 4925–4928. DOI: 10.1364/OL.44.004925. URL: https://opg.optica.org/ol/abstract.cfm?URI=ol-44-20-4925.

[Sch21] C. Schelte. “Dynamics of Optical Localized Structures in Passively Mode-Locked Lasers”. PhD thesis. Universität Münster, 2021.

[SJG22] T. G. Seidel, J. Javaloyes, and S. V. Gurevich. “A normal form for frequency combs and localized states in Kerr Gires-Tournois interferometers”. In: *Opt. Lett.* 47.12 (2022), pp. 2979–2982. DOI: 10.1364/OL.457777. URL: https://opg.optica.org/ol/abstract.cfm?URI=ol-47-12-2979.

[Str94] S. H. Strogatz. *”Nonlinear Dynamics and Chaos: With Applications to Physics, Biology, Chemistry, and Engineering”*. CRC Press, 1994.

[SWX13] J. Sheng, J. Wang, and M. Xiao. “Synchronous control of dual-channel all-optical multistate switching”. In: *Opt. Lett.* 38.24 (2013), pp. 5369–5372. DOI: 10.1364/OL.38.005369. URL: https://opg.optica.org/ol/abstract.cfm?URI=ol-38-24-5369.

[Thi] U. Thiele. *Lecture "Introduction to Numerical Continuation" Winter Term 2020/21*. DOI: 10.5281/zenodo.4544848. URL: https://dx.doi.org/10.5281/zenodo.4544848 (visited on 06/01/2024).

[Ura+11] S. Ura et al. "In-line rotation sensor based on VCSEL behavior under polarization-rotating optical feedback". In: *Opt. Express* 19.24 (2011), pp. 23683–23688. DOI: 10.1364/OE.19.023683. URL: https://opg.optica.org/oe/abstract.cfm?URI=oe-19-24-23683.

[YG14] S. Yanchuk and G. Giacomelli. "Pattern Formation in Systems with Multiple Delayed Feedbacks". In: *Phys. Rev. Lett.* 112 (17 2014), p. 174103. DOI: 10.1103/PhysRevLett.112.174103. URL: https://link.aps.org/doi/10.1103/PhysRevLett.112.174103.

Declaration of Academic Integrity

I hereby confirm that this thesis, entitled

"Dynamics of Square-Waves in Time-Delayed Kerr Micro-Cavities"

is solely my own work and that I have used no sources or aids other than the ones stated. All passages in my thesis for which other sources, including electronic media, have been used, be it direct quotes or content references, have been acknowledged as such and the sources cited. I am aware that plagiarism is considered an act of deception which can result in sanction in accordance with the examination regulations.

____

(date, signature of student)

I consent to having my thesis cross-checked with other texts to identify possible similarities and to having it stored in a database for this purpose.

I confirm that I have not submitted the following thesis in part or whole as an examination paper before.

____

(date, signature of student)